

FABRICATION OF PEROVSKITE SOLAR CELLS USING ULTRASONIC SPRAY COATING

**A Thesis Submitted to
The Graduate School of Engineering and Science of
İzmir Institute of Technology
In Partial Fulfillment of the Requirements for the Degree of
MASTER OF SCIENCE
in Photonics Science and Engineering**

**by
Eray CEYHAN**

**July 2022
İZMİR**

ACKNOWLEDGEMENTS

First of all, I would like to thank my family for their endless support.

I would like to thank my supervisor Asst. Prof. Dr. Emre SARI who always been with me at the critical points of my master study and taught me how to learn from my mistakes. The door to his office was always open whenever I ran into a trouble spot or had a question. I am very grateful for his kind personality, friendship, and guidance.

I would like to thank Assoc. Prof. Dr. Serkan ATEŞ and Assoc. Prof. Dr. Serhat TOZBURUN who are the committee members of my thesis, for their participation.

Thank you to Ümit PURÇAK whom I share the same laboratory, for being my partner in crime, friendship, and helpfulness since we worked together. I also would like to thank another laboratory mate Emre KONAN for his amazing personality, kindness, and friendship. Thank you to Hikmet Emre DEMİRTAŞ for his participation of our long hour works and support. I thank to Metin TAN for his supports and helpfulness.

I would like to thank Volkan BOZKUŞ and Hakan BOZURT who are working at our neighboring laboratory, for their friendship. I would like to thank Sema SARISÖZEN, Tufan AKKAN and Canan ÖZTAŞKIN for being amazing neighbors and friends.

Finally my biggest thanks to my girlfriend Remziye YILDIZ for always being there for me.

ABSTRACT

FABRICATION OF PEROVSKITE SOLAR CELLS USING ULTRASONIC SPRAY COATING

Perovskite solar cells (PSCs) are one of the most prominent research field for the last decade in photovoltaic technology. From 3.8 percent in 2009 to 25.7 percent in 2021 in single-junction architectures, and to 29.8 percent in silicon-based tandem cells, solar cell efficiencies of laboratory-scale devices using these materials have increased, surpassing the maximum efficiency achieved in single-junction silicon solar cells. Therefore, as of now, perovskite solar cells represented the solar technology that was developing the fastest. Perovskite solar cells have gained commercial appeal thanks to their extremely low production costs and promise for even higher efficiency. Their short- and long-term stability are key issues and research topics.

In this context, the development of scalable perovskite solar cell fabrication has become essential. A novel ultrasonic spray casting technique is employed by incorporating hot nitrogen gas blowing as a scalable deposition method. We tried to optimize the perovskite film crystallization by applying our technique. With the help of our hot nitrogen gas blowing pipe we are able to enhance the nucleation process and at a desired levels. These investigations are supported by characterization tools such as optical microscope, scanning tunneling microscope, and current-voltage measurement.

$\text{MAPb}(\text{I}_{1-x}\text{Br}_x)_3$ precursor solution containing DMF and DMSO as solvent was used in our experiments. We examined the effect on the surface roughness change by adjusting the DMF and DMSO ratios.

Finally, we construct a device of FTO/ c-TiO₂/ m-TiO₂/ $\text{MAPb}(\text{I}_{1-x}\text{Br}_x)_3$ /Spiro-OMeTAD/Au architecture and able to investigate the electrical characteristic of under dark and illumination.

ÖZET

ULTRASONİK SPREY KAPLAMA YÖNTEMİ İLE PEROVSKİT GÜNEŞ HÜCRELERİNİN FABRİKASYONU

Perovskit güneş hücreleri (PGH'ler), fotovoltaik teknolojisinde son on yılın en önde gelen araştırma alanlarından biridir. 2009'da yüzde 3,8 den 2021'de tek eklemli mimarilerde yüzde 25,7'ye ve silisyum bazlı tandem hücrelerde yüzde 29,8'e, perovskit malzemeleri kullanan laboratuvar ölçekli aygıtların güneş verimlilikleri tek eklemli silisyum güneş hücrelerinin verimliliklerini aşarak artı. Bu nedenle, şu an itibarıyle perovskit güneş pilleri, en hızlı gelişen güneş teknolojisini temsil ediyor. Perovskite güneş pilleri, son derece düşük üretim maliyetleri ve daha da yüksek verimlilik vaatleri sayesinde ticari çekicilik kazanmıştır. Kısa ve uzun vadeli istikrarları kilit konular ve araştırma konularıdır.

Bu bağlamda, ölçülebilir perovskite güneş pili üretiminin geliştirilmesi elzem hale geldi. Ölçülebilir bir kaplama yöntemi olarak sıcak nitrojen gazı üfleme dahil edilerek yeni bir ultrasonik sprey döküm tekniği kullanıldı. Tekniğimizi uygulayarak perovskite film kristalizasyonunu optimize etmeye çalıştık. Sıcak nitrojen gazı üfleme borumuz sayesinde nükleasyon sürecini istenilen seviyelerde iyileştirmektedir. Bu araştırmalar optik mikroskop, taramalı tünelleme mikroskopu ve akım-voltaj ölçümü gibi karakterizasyon araçlarıyla desteklendi.

Deneylerimizde çözücü olarak DMF ve DMSO içeren $\text{MAPb}(\text{I}_{1-x}\text{Br}_x)_3$ öncü çözeltisi kullanıldı. DMF ve DMSO oranlarını ayarlayarak yüzey pürüzlülüğü değişimi üzerindeki etkisini inceledik.

Son olarak, FTO/c-TiO₂/m-TiO₂/ $\text{MAPb}(\text{I}_{1-x}\text{Br}_x)_3$ /Spiro-OMeTAD/Au mimarisine sahip bir cihaz inşa ettik, ve karanlık ve aydınlatma altında elektriksel özelliklerini araştırabilildik.

TABLE OF CONTENTS

LIST OF FIGURES	viii
LIST OF TABLES	x
LIST OF ABBREVIATIONS.....	xi
CHAPTER 1. INTRODUCTION	1
CHAPTER 2. PEROVSKITES FOR PHOTOVOLTAICS.....	5
2.1. Crystal Structure	5
2.1.1. Cubic, Tetragonal, Orthorhombic Structure.....	5
2.1.2. Goldschmidt Tolerance Factor	7
2.1.3. X-Ray Diffraction Patterns.....	7
2.2. Electronic Structure.....	8
2.2.1. Molecular Orbitals and Band Structure.....	9
2.2.2. Band Gap Size	10
2.3. Carrier Dynamics	11
2.3.1. Absorption, Photogeneration, and Exciton Binding Energy	11
2.3.2. Lifetime and Recombination Processes.....	12
2.3.3. Photoluminescence Quantum Efficiency	13
2.4. Mechanical Properties.....	14
CHAPTER 3. ORGANIC INORGANIC HALIDE PEROVSKITE SOLAR CELL	16
3.1. Solid-State Device Theory	16
3.1.1. Valence and Crystal Structure	16
3.1.2. Band Theory of Solids.....	17
3.1.3. Electrons and Holes.....	18
3.1.4. P-N Junction	19
3.2. Solar Cell.....	20
3.2.1. Equivalent Circuit of a Solar Cell	20

3.2.3. I-V Characteristics of Solar Cell	22
3.2.4. Efficiency Measurement of a Solar Cell	24
3.2.5. Shockley-Quieser Limit.....	25
3.3. Organic Inorganic Halide Solar Cell.....	26
3.3.1. Basic Optic Properties	26
3.3.2. Fabrication and Working Principle	28
3.3.3. Crystallization.....	29
3.3.4. Deposition Techniques	31
3.3.5. Spray Coating	34
CHAPTER 4. EXPERIMENTAL METHODOLOGY	39
4.1. Novel Spray Deposition System	39
4.2. Perovskite Solar Cell Fabrication.....	42
4.2.1. Etching.....	42
4.2.2. Cleaning.....	43
4.2.3. Electron Transport Layer.....	43
4.2.4. Perovskite Layer	43
4.2.5. Hole Transport Layer	44
4.2.6. Gold Contact.....	44
4.3. Characterization	45
4.3.1. Optical Microscopy	45
4.3.2. Scanning Electron Microscope.....	46
4.3.3. X-Ray Diffraction.....	46
4.3.4. Current-Voltage Measurement	47
CHAPTER 5. RESULTS AND DISCUSSION.....	49
5.1. Morphology of Perovskite Thin Films	49
5.2. Precursor Solution.....	51
5.3. Crystallization and Electrical Characteristic of Perovskite Films.....	53

5.4. Further Development of Spray Coating System	55
CHAPTER 6. CONCLUSION	57
REFERENCES	58

LIST OF FIGURES

<u>Figure</u>	<u>Page</u>
Figure 2.1. Perovskite Lattice Structure	6
Figure 2.2. XRD patterns of $\text{FA}_{1-x}\text{Cs}_x\text{PbI}_3$ with varying Cs compound	8
Figure 2.3. Computationally calculated band structure of CsPbBr_3	9
Figure 2.4. Band gaps of perovskite materials with respect to applied pressure	10
Figure 2.5. Time-resolve PL (left). The transient-absorption spectroscopy (right).....	12
Figure 2.6. Rate of recombination with respect to carrier concentration	13
Figure 2.7. PLQE measurement to detect the maximum achievable quantum efficiency.....	14
Figure 3.1. Band gap of the metal, semiconductor, and insulator.....	17
Figure 3.2. Electron and hole charge carriers through doping.....	18
Figure 3.3. P-N junction.	19
Figure 3.4. Basic working principle of a simple solar cell	20
Figure 3.5. The equivalent solar cell circuit model under illumination.....	21
Figure 3.6. Current and voltage (I-V) curve of a solar cell.	23
Figure 3.7. Fill factor of solar cell	24
Figure 3.8. Shockley-Queisser limit maximum efficiency of one p-n junction solar cell.....	25
Figure 3.9. Solar spectrum losses of Si solar cell	26
Figure 3.10. Wavelength tuning for MAPb halide perovskite with respect to Br	27
Figure 3.11. Various device architectures of perovskite solar cell	28
Figure 3.12. Energy diagram for PSC.....	29
Figure 3.13. Representative process of nucleation and grain growth	30
Figure 3.14. Different grain sizes with respect to precursor solution temperature.....	31
Figure 3.15. Basic spin coating process.....	32

<u>Figure</u>	<u>Page</u>
Figure 3.16. Blade and slot-die coating	33
Figure 3.17. Inkjet printing technique	33
Figure 3.18. Screen printing	34
Figure 3.19. Illustration of spray-coating procedure	35
Figure 3.20. Illustration of two step ultrasonic spray	36
Figure 3.21. Schematic illustration mechanism for the spray-coating process	37
Figure 4.1. Types of nozzles.....	39
Figure 4.2. Top and side view illustration of the nozzle.....	40
Figure 4.3. (a) Hot N ₂ gas carrier, (b) dynamic spray system	40
Figure 4.4. The whole system of the spray cast deposition.....	41
Figure 4.5. Etching process.....	42
Figure 4.6. CH ₃ NH ₃ PbI _x Br _{1-x} solar cells.	45
Figure 4.7. Slot and PCB.Purple and yellow boxes touching gold and FTO respectively.....	47
Figure 4.8. Abet 11002 SunLite solar simulator and Keithley 2400 source meter.....	48
Figure 5.1. Optical microscopy images of perovskite film under illumination from (a) bottom, (b) up, scalebar represents 200 μm.....	50
Figure 5.2. SEM images of perovskite films with different distances.....	51
Figure 5.3. Cross-section SEM images.....	52
Figure 5.4. (a) and (b) dark and illuminated J-V, (c) and (d) dark and illuminated I-V curves respectively.....	54
Figure 5.5. P-V Characteristics of perovskite solar cell.....	55

LIST OF TABLES

<u>Table</u>	<u>Page</u>
Table 2.1. Some mechanical properties of halide perovskites.....	15
Table 5.1. Parameters of champion solar cell.....	55

LIST OF ABBREVIATIONS

Au	Gold
DMF	Dimethylformamide
DMSO	Dimethyl Sulfoxide
ETL	Electron Transport Layer
FTO	Fluorine-Doped Tin Oxide
HTL	Hole Transport layer
CB	Conduction Band
FF	Fill Factor
VB	Valence Band
MA	Methylammonium
PV	Photovoltaic
PSC	Perovskite Solar Cell
PLQL	Photoluminescence Quantum Yield
SEM	Scanning Electron Microscope
TRPL	Time Resolved Photoluminescence
XRD	X-ray Diffraction

CHAPTER 1

INTRODUCTION

For over two and a half centuries, since the industrial revolution began, mankind has been using fossil fuels in order to meet the energy demand of the exponentially growing human population. Fossil fuels are natural resources that are formed by the remnants of the living organisms who lived in the geological past. Petroleum, coal, natural gas are the most common examples of fossil fuels. These sources are mostly burned to obtain energy; however these processes have several drawbacks both in production and in usage. Many of these sources are environmental pollutants. They are the major factor for the emission of greenhouse gases (CO_2 , CH_4 , N_2O) and consequently cause global warming and climate change. Economic and sustainability-related challenges are also present since the prices of fossil fuels fluctuate greatly due to supply and demand issues¹.

By the end of the 19th century, electricity has started to take a crucial place in modern-day society. The demand for electricity both in industry and residential settlements has grown rapidly. Since then, electrical production has been mostly done by using mostly fossil fuel-based resources. Considering the depletion of these resources and the incapability to meet the electrical energy need of humanity, renewable energy sources have become viable alternatives. Researchers and engineers around the globe grew interest in renewable and clean resources after recognizing the importance of resolving these issues.

Due to the awareness on the importance of renewable energy sources, governments, companies, as well as other different institutions and organizations, are now making vast amounts of investments in diverse clean and renewable energy sources. Wind, hydropower, geothermal, biomass and solar energy are known and widely used resources of renewable energy and subsequent conversion to electrical energy. All of these sources are prominent in terms of electrical energy generation by their own means. On the other hand, solar energy seems to be of paramount importance

over other renewable resources considering the amount and continuity of sunlight we have. Those obvious advantages of solar energy have the ability to address the environmental, economic and political challenges associated with electricity generation.

Solar cells are at the center of electricity generation in photovoltaic (PV) modules. A solar cell is a device that converts the energy of sunlight into an electrical power by employing the photovoltaic (PV) effect. Solar cells comprise of semiconductor materials as the light-absorbing material that has a certain band gap energy. When incident photons of sunlight reach the solar cell, some of its energy is absorbed by the semiconductor material of the cell and generates electrical charges in regard to an electric field in the cell resulting in the flow of electricity. The key metric of a solar cell is its power conversion efficiency (PCE) characterized by the ratio of the incident energy of sunlight to generated energy of solar cell.

Since their inception in 1954 in Bell Labs, solar cells have been fabricated by optimizing in a cost-effective way. The cost-effectiveness of the solar cell is defined by their price in per unit power (\$/watt). The lower this ratio means better cost-effectiveness of the solar cell. Starting from the second half of the 1970s, \$/watt ratio descended from 76.00\$ to 0.30\$ in mid 2010s². Although this indicates an important progress, this ratio should be lesser than 0.30\$ in order for solar cell technology to be a feasible option.

Solar energy, however, is still used far below its potential. Solar cells have several barriers to using solar energy, such as low efficiency and high cost. Researchers have been investigating varied materials and device structures in order to overcome these issues. In most solar cells today, a number of active semiconductor materials are present such as Cadmium Telluride (CdTe)³, Gallium Arsenide (GaAs)⁴, Copper Indium Diselenide (CIS)⁵, and Silicon (Si)^{6,7}. At the same time, numerous novel materials have recently been introduced to use in solar cell applications namely quantum dots^{8,9}, organic/polymer materials^{10–13}, and dye-synthesized materials¹⁴.

As of now, silicon is by far the most common semiconductor material used in PV technologies because of its cost-efficiency, resistance to corrosion, non-toxicity, long-term durability, and photosensitivity. It is also the most abundant element after oxygen on the earth's crust. Silicon is reaching its upper theoretical limit known as the Shockley-Queisser limit¹⁵ although having those advantages. Silicon-based PV

technology also suffers from high cost and low efficiency. As a result of these, scientists are devoted to exploring and producing new types of materials.

The perovskite materials which have a crystal structure of any material ABX_3 where A and B is cation each and X is an anion that bonds to both. They are one of the most promising semiconductor materials for the next-generation PV cells. It was first discovered and named by Russian mineralogist L.A. Perovski in the Ural mountains of Russia in 1839 as the mineral calcium titanium oxide ($CaTiO_3$). Although the discovery of perovskite dates back to two centuries ago, its importance and potential for solar cell applications have yet been understood for just over a decade.

In an effort to confront the challenges of the future generation solar cells, the organic lead halide perovskites emerged as an important candidate thanks to their superior performance, high efficiency, long carrier diffusion length, charge transfer mechanism, high optical absorption coefficient and defect tolerance. Realization of the exceptional properties of organic lead halide perovskite materials make them an intense research topic in both academia and industry¹⁶⁻¹⁸.

Another key parameter for perovskite solar cells is of course their manufacturing processes. With the first synthesis and construction on a lab-scale PSCs, comes with the question of how to deposit and fabricate them. Novel techniques must be introduced for the mass production of PSCs. Many deposition methods have been employed including blade coating, slot-die, stamping, vacuum evaporation, spin coating, etc. to coat perovskite materials. Deposition processes are linked to two important parameters: their morphology and mass manufacturing. Morphology of organic lead halide PSCs is vital in order to obtain high-efficiency films. The power conversion efficiency measured correlates with the quality of the perovskite films in devices. Similarly, the deposition technique is also crucial for fabricating those solar films since the ultimate purpose for these materials is their feasibility in industry and residential usage. Hence to find a commercial purpose for organic lead halide perovskite solar cells it is essential to establish wide-area coating process for the creation of uniform films as the main innovation for attaining high efficiency in such cells rely on the formation of homogenous perovskite films

To address these challenges mentioned above, the spray coating technique is a novel and promising method. It is cost-effective, ready-to-use, and maybe most

importantly could coat large areas. The ability to cover larger solar modules is critical for the purpose of sustainability of this technique since conventional techniques lack of doing so.

In this context, in this thesis, our hypothesis is “active absorbing perovskite layers of PSCs can be deposited *via* spray coating technique by controlling key parameters to optimize their crystal quality in a laboratory environment”.

CHAPTER 2

PEROVSKITES FOR PHOTOVOLTAICS

Perovskite-based solar cells have become a game changer in the photovoltaic performance race, with quick advancement toward a power conversion efficiency over 25%¹⁹. Optical and electronic properties light absorbers are critical for understanding their interaction with light, as well as the transport and collection of photogenerated charges. Furthermore, the recombination processes must be thoroughly understood in order to maximize charge-collection efficiency and achieve the best PCE. This chapter summarizes physical, chemical, and material properties of organic halide perovskites that are quite relevant to their application in solar cells.

2.1. Crystal Structure

It is important to perform an analysis of how the atomic structures of the perovskite effect important parameters of perovskites. This chapter summarizes and describes the atomic structures of perovskite halide crystals

2.1.1. Cubic, Tetragonal, Orthorhombic Structure

The general chemical formula for halide perovskite materials used in most photovoltaics is ABX_3 where A is a monovalent cation, B is a divalent cation, and X is a halide anion. These ions are positioned in a three-dimensional system of octahedral components, with a B cation located at the center of each octahedron and an X anion is located at each of the octahedron's six corners. The network is made up of adjacent octahedra that share corners because each X anion is coupled to two B cations. Twelve

of the nearest X anions surround the bigger A cation, which is enclosed in cages created by sets of eight adjacent octahedra in the network (Figure 2.1).

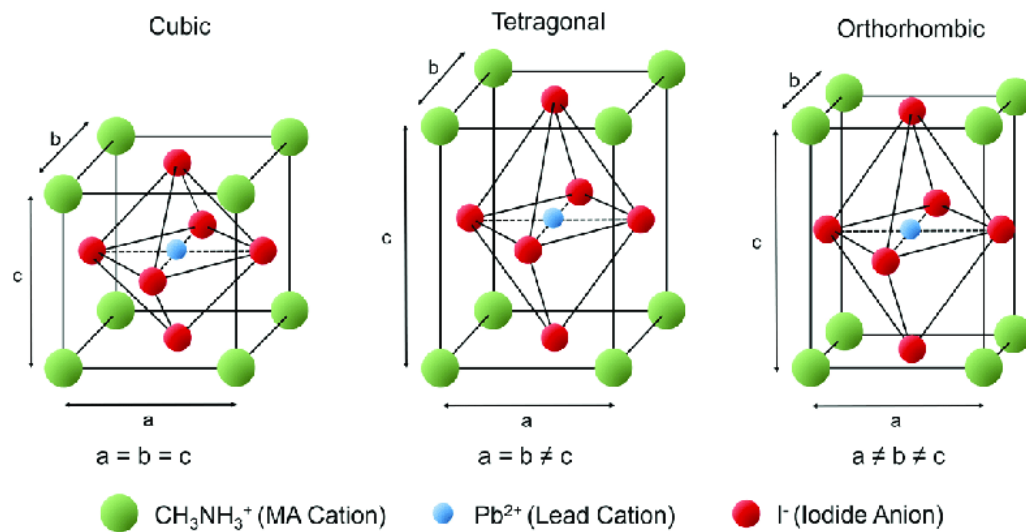


Figure 2.1. Perovskite Lattice Structure²⁰

The perovskite structure is cubic and has the space group Pm3m in its most symmetric form. When heated sufficiently, most halide perovskites adopt this configuration. Even though the A-site cation has lower symmetry, the perovskite structure is often correctly portrayed as cubic because at room temperature, this ion rotates freely, becoming a cubic-like symmetry²¹

Lower temperatures cause halide perovskites to phase transition to a lower symmetry tetragonal phase, and still lower temperatures cause an orthorhombic phase to form. These structural transitions can be thought of as the result of adjacent octahedra swaying or rotating slightly relative to one another while maintaining connectivity at the corners, starting with a cubic crystal (Figure 2.1). The Glazer notation system offers a method to identify correctly for every type of tilt that is possible. It accomplishes this by clarifying which axis or axes the tilt takes place around and which orientation octahedra change direction in relation to adjacent octahedra²²

The cubic unit cell's lattice constants are typically in the range of 5.95 Å to 6.40 Å, with trends that usually follow the size of the ions in the perovskite. When the common and fairly large organic cation formamidinium (FA) is replaced with the smaller Cs, the lattice shrinks isotropically or by tilting the octahedra, resulting in a

distortion to the tetragonal phase. The effects of compositional replacement on the band gap and band positions of the perovskite-isotropic lattice contraction increase molecular orbital interaction, pushes conduction and valence bands upward, and shrinks the band gap, whereas octahedral tilting decreases molecular orbital interaction, pushes the bands downward, and increases the band gap.

2.1.2. Goldschmidt Tolerance Factor

The relative sizes of A, B, and X ions are constrained by geometrical limit in order for them to arrange in perovskite crystalline structure. As defined in equation 2.1, Goldschmidt tolerance factor assesses the geometric stability and distortion of crystal structures.

$$t = (r_A + r_X)/\sqrt{2}(r_B + r_X) \quad (2.1)$$

A tolerance factor of 1 would be provided by ions of the perfect size to fit cozily in the network of octahedra. Empirical evidence suggests that groups of ions with tolerance factors between 0.8 and 1.0 are more willing to form the perovskite structure²³. A non-perovskite phase occurs if ABX_3 compounds do not meet this criterion.

2.1.3. X-Ray Diffraction Patterns of Perovskites

In the XRD analysis of the perovskite structures, one needs to be clarified is that the term crystallinity. For example, a diffraction peak's area should be strongly linked with the quantity of crystalline phase present. The thickness and texture also affect peak area. Moreover, the peak width is influenced by finite crystallite size and structural flaws such as dislocations and stacking faults²⁴

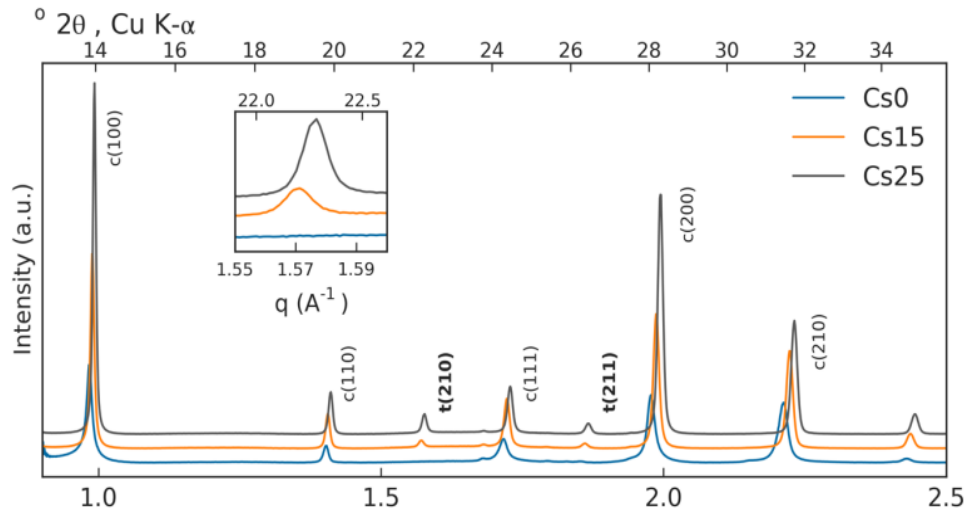


Figure 2.2. XRD patterns of $\text{FA}_{1-x}\text{Cs}_x\text{PbI}_3$ with varying Cs compound²⁵

Figure 2.2 depicts an exemplary XRD patterns of cubic and tetragonal metal halide perovskite thin films. It is easily identified that the peak corresponds to the (100) plane is for cubic perovskite. Additional superlattice peaks emerges in the XRD patterns after partial replacement at positions corresponding to half-integer values of Miller indices, denoting that a tetragonal distortion and lowering of symmetry caused by tilting of PbI_6 octahedra that comprise the perovskite crystalline structure. For tetragonal perovskites, when compared to cubic perovskite, the unit cell is adequately doubled (Figure 2.1). As a result, more XRD peaks are observed.

2.2. Electronic Structure of Perovskites

An overview of findings involving measurements of the electronic structure of hybrid perovskites is intended by this section. Both computational and experimental results from the literature have been presented to give better insight of the electronic structure of perovskite materials.

2.2.1. Molecular Orbitals and Band Structure

Combination of metallic and halogen atomic orbitals which have characteristic patterns form perovskite semiconductors a vital feature: a direct band gap that can be tuned through compositional replacement and high tolerance to crystal defects or surface states.

The valence band maximum of ionic ABX_3 metal halide perovskites is an antibonding hybrid state of the metal s and halide p orbitals, whereas the conduction band minimum with less antibonding and more nonbonding character, is a hybrid of metal p and halide p orbitals^{26,27}. Because the valence band maximum is made up of antibonding configurations of metal s and halogen p orbitals, any transition to the perovskite lattice that increases the amount of metal-halide overlap distorts the valence band and raises its energy. The conduction band, which is derived from p orbitals and has less orbital overlap, is expected to react less strongly to lattice structure deformations than the valence band, which originates from metal s orbitals.

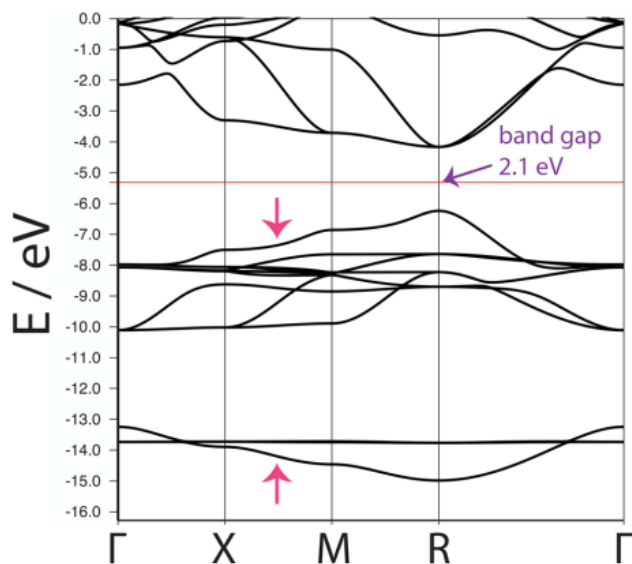


Figure 2.3. Computationally calculated band structure of CsPbBr_3 ²⁸

2.2.2. Band Gap Size

Several factors play role on the formation of band structure. Perovskite bulks require enough doping concentration, known as alloying, to cause localized impurity states to interact with each other and the host states in order to successfully change the bandgap. This alloying technique is widely used to tailor the electronic structure, with the final bandgap having a roughly quadratic dependence on the molar ratio of one component²⁹.

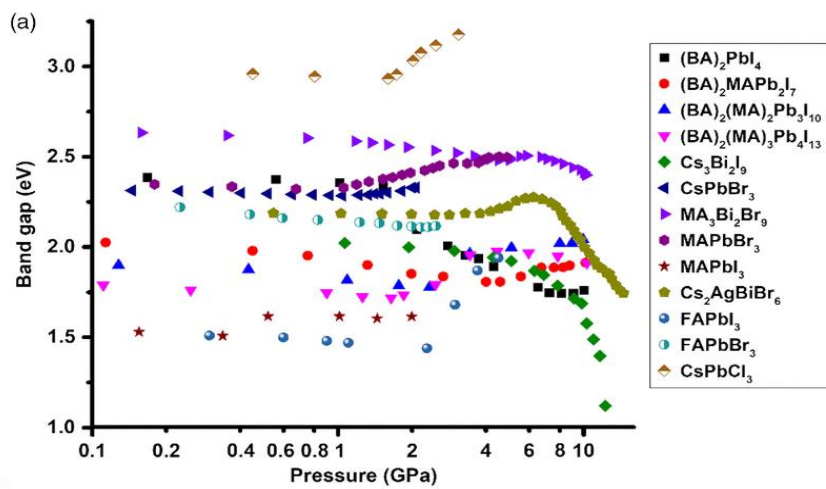


Figure 2.4. Band gaps of perovskite materials with respect to applied pressure³⁰

Pressure also has the ability to substantially impact the energy band structure of semiconductors by compressing the lattice constants, modifying the lattice structure (distorting, titling, or rotation), and inducing complex phase transitions, which change the boundary conditions of wave functions and affect the bandgap (Figure 2.4).

Indirect to direct band gap transition is possible via dimensional reduction. Because the partial introduction of too large A-site impurities causes dimensional reduction, the indirect to direct band gap transition can be realized by assembling 2D or 1D crystals to change the energy band structure and achieve indirect–direct-gap crossover³¹.

2.3. Carrier Dynamics

The rates of generation and recombination of free charge carriers in halide perovskites has been examined extensively by transient spectroscopic techniques. Distinguished study by Herz³² and many others asked the main questions. In this section, we briefly discuss major findings on which there is an agreement.

In photovoltaics, photons with a sufficient energy generating electron-hole pair in semiconductor absorber is called photogeneration. It takes place in picosecond³³. Because exciton binding energies are comparable to thermal energy³². Through phonon interactions, generated carrier thermalizes and cool ranging from picoseconds to hundreds of picoseconds³³. In particular, the rate of recombination and the proportion of radiative recombination phenomena are profoundly important factors that determine solar cell carrier extraction and open circuit voltage. What happens to free thermalized electrons and holes over the interval of nanoseconds to microseconds is vital to the operation of solar cells. In an efficient solar cell absorbing material, these photogenerated carriers are collected in a way that to produce high open circuit voltage.

2.3.1. Absorption, Photogeneration, and Exciton Binding Energy

The quantized exciton Landau levels in the absorption spectra of formamidinium and methylammonium lead iodide perovskites were used to measure the exciton binding energies, which were found to be 10–12 meV³⁴. When photons having energies larger than the band gap energy of the material are absorbed, free carriers are created. Excitonic effects become noticeable at cryogenic temperatures, and one such effect is a prominent absorption peak that develops near the band edge as a result of absorption into bound excitonic states³⁵.

The absorption coefficient is significantly increased by the Coulomb attraction between excited electrons and holes even at room temperature³⁶. The final state of the absorption process is stabilized to some extent by coulombic interaction between holes in the valence band and electrons in the conduction band, strengthen the absorption. In comparison to the coefficient predicted by first principles calculations presuming free

carriers with no Coulomb interaction, Davies et al. have demonstrated an improvement in the absorption coefficient of MAPbI_3 and a sharpening of the absorption start^{36,37}.

2.3.2. Lifetime and Recombination Processes

At various amounts of the charge carrier density produced by excitation, recombination processes in halide perovskites exhibit different regimes (Figure 2.5).

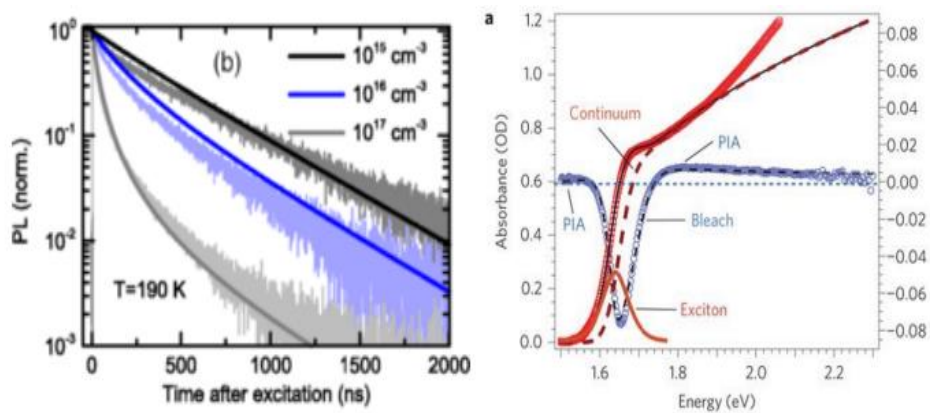


Figure 2.5. Time-resolve PL (left)³⁸. The transient-absorption spectroscopy (right)³³.

With lifetimes ranging from tens of nanoseconds to a few microseconds photoluminescence intensity decays and/or the intensity of the ground state lightens in transient absorption are often monomolecular having lifetimes in the time interval of tens of nanoseconds to a few microseconds. A thorough investigation by Richter et al. demonstrates that for a MAPbI_3 film produced in a manner that results in a greater photoluminescence quantum efficiency, the conversion from monomolecular to bimolecular dependence happens at a substantially lower carrier density. Studies repeatedly demonstrate that as excitation density is increased from the monomolecular to the bimolecular regime, the photoluminescence quantum efficiency dramatically increases, which is consistent with the fact that the majority of recombination is radiative³⁸.

Since the TA signal reflects all free carriers present and decays as a result of every recombination process, examination of decays in transient absorption (TA)

provides the entire rate of recombination. On the other hand, analysis of transient photoluminescence (TRPL) exclusively examines radiative recombination events. Figure 2.6 depicts a plot of recombination rate versus excitation density produced from TA and TRPL.

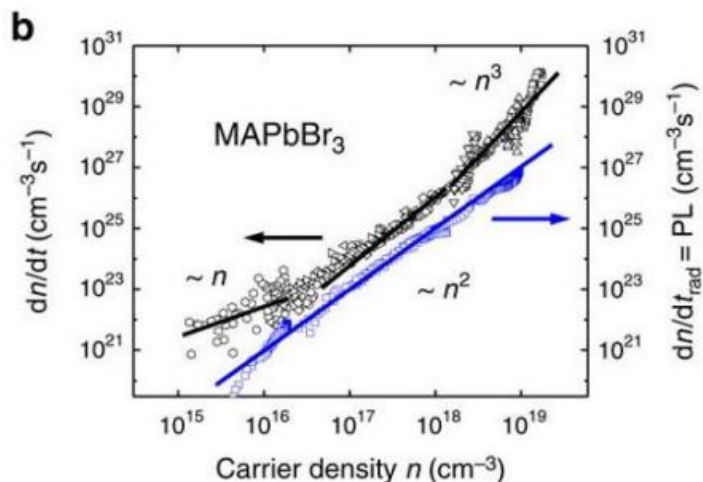


Figure 2.6. Rate of recombination with respect to carrier concentration³⁹.

2.3.3. Photoluminescence Quantum Efficiency

High photoluminescence quantum efficiencies (PLQE) polycrystalline material produced at low temperatures is a distinguishing feature of hybrid halide perovskite semiconductors. Many techniques have been successfully used to further increase radiative efficiency, including light soaking in dry or humid air⁴⁰, treatment with Lewis bases like pyridine and thiophene⁴¹, and treatment with dipolar ligands like trioctylphosphine oxide (TOPO)⁴².

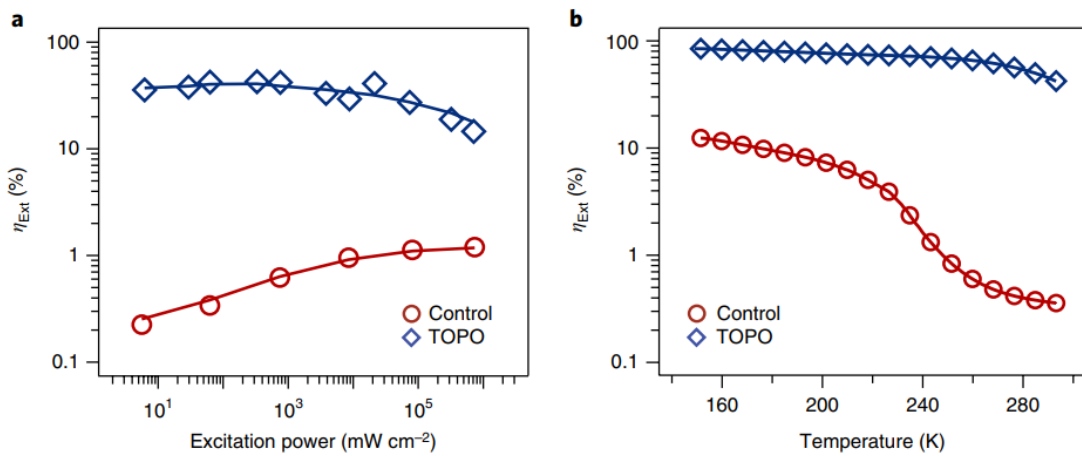


Figure 2.7. PLQE measurement to detect the maximum achievable quantum efficiency⁴³

The PLQE of a complete device, where the perovskite is sandwiched between electron-and hole-selective contacts, the PLQE that is directly related to solar cell open circuit voltage, despite the fact that remarkable PLQEs have been recorded in bare films of perovskite on insulating glass substrates.

To boost device PLQEs to the levels regularly achieved by bare perovskite films, it is critical to identify the mechanisms of nonradiative recombination in complete solar cells and reduce them. Recently, methods that increase the PLQE or ELQE of a whole device have been successfully employed in reports of perovskite solar cells with high open circuit voltage to produce better open circuit voltages⁴⁴.

2.4. Mechanical Properties

There are two main differences between the mechanical characteristics of hybrid organic-inorganic perovskite (HOIP) materials with ABX_3 structures and those of their oxide equivalents⁴⁵. One is that the huge variety of organic molecules can be used to modify the mechanical characteristics of HOIPs to yield the desired assembly. The other one is that the crystal structure's additional degrees of freedom also give HOIPs a lot of mechanical flexibility.

Table 2.1. Some mechanical properties of halide perovskites⁴⁹.

Property	Value	Notes
Coefficient of thermal expansion	$42 - 50 \times 10^{-6} \text{ C}^{-1}$	X-ray diffraction ^{46,47}
Young's modulus	10-20 GPa	Nanoindentation ^{46,48}
Hardness	0.4-0.6 GPa	Nanoindentation ⁴⁶
Cohesive fracture resistance	$1-2 \text{ J m}^{-2}$	Double cantilever beam ⁴⁷

For MAPbX_3 , Young's moduli between 10 and 20 GPa have been recorded using nanoindentation tests on single crystals. As the halogen group is moved up from iodide to bromide and subsequently chloride, Young's modulus increases⁴⁸ (Table 2.1).

In thin film or single crystal forms, MAPbI_3 exhibits a significant linear thermal expansion coefficient of 42 to $52 \times 10^{-6} \text{ K}^{-1}$. A thin film of perovskite manufactured on a glass substrate will undergo significant in-plane thermal stresses at any temperature other than the temperature at which the perovskite film crystallized on that substrate due to the fact that this is greater than the thermal expansion coefficient of soda lime glass by a multiplying factor of five⁵⁰. Perovskite films that have been solution-deposited often crystallize higher than room temperature, typically between 100 and $150 \text{ }^\circ\text{C}$. The perovskite layer and the substrate tend to compress in different ways when the temperature at which crystallization takes place is cooled to room temperature, and the substrate prevents the thin film from contracting. As a result of this even after the film has crystallized and cooled, there is still a tensile stress present. It has been demonstrated that the presence of residual tensile strain speeds up the conversion of MAPbI_3 to PbI_2 . This is most likely because a tensile strained film has a lower activation energy barrier for charge transfer.

Overall, the study of perovskite mechanics is still in its early stages. Given the difficulties associated with perovskite usage, it is likely that research into these materials' mechanical properties will continue to expand and combine knowledge from a variety of disciplines.

CHAPTER 3

ORGANIC INORGANIC HALIDE PEROVSKITE SOLAR CELL

3.1. Solid-State Device Theory

This section covers the summary of physical knowledge of the solids-state devices. In order to comprehend perovskite solar cells and solar cells in general basic phenomena of the solid-state physics of the p-n junctions need to be understood.

3.1.1. Valence and Crystal Structure

Electrons that are located valence or outermost shell called valence electrons. They are responsible of the chemical properties of the material. These electrons are the ones that interact chemically with other elements. Atoms may lose a few electrons to reveal a complete shell underneath. A few electrons may be accepted by an atom to fill its shell.

The elements that have the ability easily give away their electrons are called conductors. For instances Li, Na, K, Cu, Ag, and Au are all group I elements having a single electron in their valence shell, and they have similar chemical properties.

There are 7 electrons in the outer shell of the Group VIIA elements Fl, Cl, Br, and I. These substances will happily accept one additional electron, giving their outer shell a total of 8 electrons. These elements which do not give electrons called insulators.

Group IVA elements C, Si, and Ge which are semiconducting, create compounds by exchanging electrons with other elements without creating ions. These elements have four electrons in their valence shells. Covalent bonding is the name for

this shared electron bonding. By sharing electrons, the center atom (and the others by extension) have finished forming their valence shells.

A crystal is an orderly arrangement of atoms (or ions) that forms in the majority of inorganic substances. Atoms' valence shell clouds interact in a predictable way. At the tiniest level, even metals are made of crystals.

3.1.2. Band Theory of Solids

According to the four-fold system of quantum numbers, quantum physics explains the states of electrons in an atom. The permissible states that electrons in an atom may adopt are described by the quantum numbers.

An external source of extra energy must be provided to the electron to allow it to enter a higher-order shell. An electron loses some of its energy as it "leaps" into a lower shell, on the other hand.

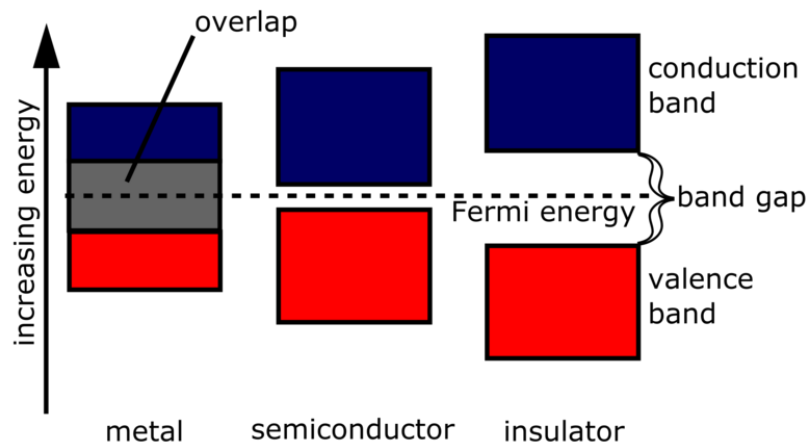


Figure 3.1. Different size of band gap of the metal, semiconductor, and insulator⁵¹.

Metals require little energy to remove an electron because the valence and conduction bands intersect. Metals therefore are superb conductors. An insulator's wide valence-conduction band gap necessitates significant energy to expel an electron. As a result of this insulators are not conductive. On the other hand, the valence and conduction bands in semiconductors have a very small, non-overlapping gap between

them. So pure semiconductors are neither good insulators nor conductors, the word itself is made up of from the combination of words semi and conductor.

3.1.3. Electrons and Holes

Electrons and electron holes are free charge carriers in semiconductors. Excitation of an electron from the valence band to the conduction band yields electrons and holes. A hole or electron hole in an atom or atomic lattice is the absence of an electron in a place where it should be present. It is one of the two types of charge carriers that are responsible for creating electric current in semiconducting materials

Pure semiconductors generally are not specifically useful on their own. In regard to Si by doping with an electron donor like phosphorus, it is possible to increase the number of negative charge carriers in semiconductor material. Nitrogen, phosphorus, arsenic, and antimony are elements from group VA of the periodic table are used to add to obtain desired impurity by giving its electrons also known as n-type doping.

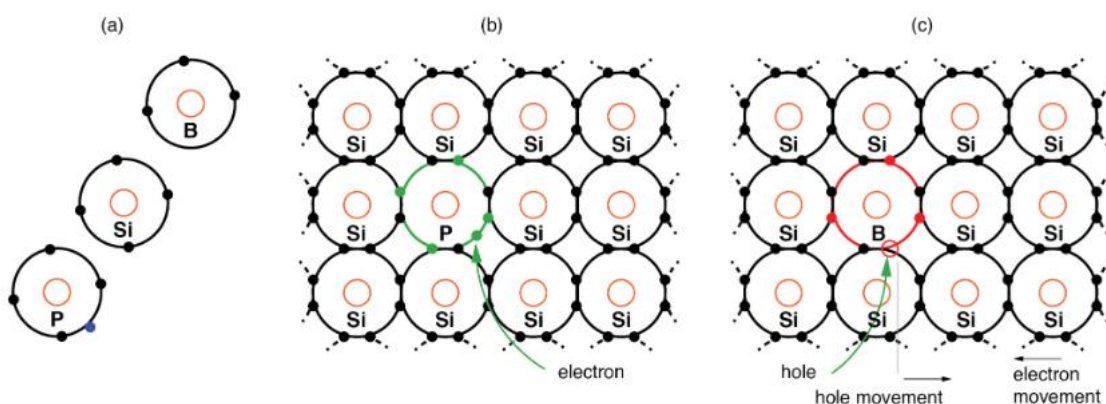


Figure 3.2. Electron and hole charge carriers through doping⁵².

In p-type doping, dopants are usually boron or gallium. Each of the outer orbitals of these elements contains three electrons. They create "holes" in the silicon atoms' valence band when they are incorporated into the silicon lattice. As a result, the valence band's electrons gain mobility, and the holes migrate in the opposite direction of the electrons. Only positive charges are able to migrate because the dopant is bound in the

crystal lattice. These semiconductors are referred to be p-type because of the positive holes.

3.1.4. P-N Junction

A monocrystalline semiconductor having both a p-type and an n-type region close by at a junction is used to create p-n junctions. There are certain special characteristics of a single semiconductor crystal constructed with p-type material at one end and n-type material at the other.

Positive majority charge carriers, or holes, are present in the p-type material and are able to move freely through the crystal lattice. Electrons, the mobile negative majority carriers, are present in n-type materials. Electrons from n-type materials diffuse over the junction in the vicinity and combine with holes from p-type materials.

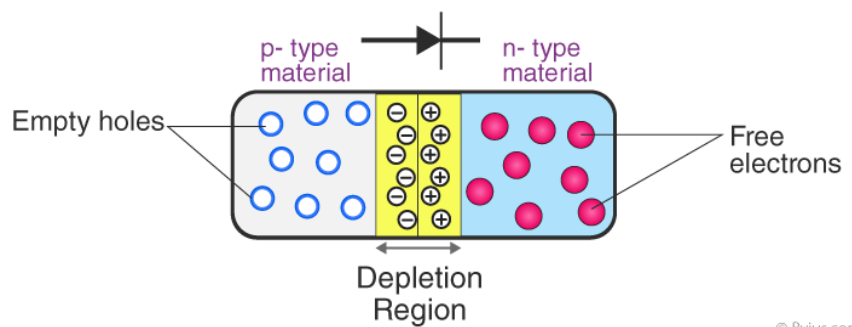


Figure 3.3. P-N junction⁵³.

The depletion area is the thin layer of the crystal lattice between these charges that has had its majority carriers removed. It changes into intrinsic semiconductor material that is not conductive. The conductive p and n doped areas are effectively separated by the depletion region. A potential barrier is created by the separation of charges at the p-n junction. For the junction to conduct, this potential barrier needs to be overcome by an external voltage source.

Once the barrier voltage is passed, a forward-biased p-n junction starts to conduct a current. Current flow is made possible by recombination, which is forced

toward the junction by the externally applied potential. Nearly no current flows through a reverse biased p-n junction. Reverse bias is applied, drawing most carriers away from the junction. The nonconducting depletion area becomes thicker as a result.

3.2. Solar Cell

French physicist Edmond Becquerel was the first to experimentally show the photovoltaic phenomenon. He created the first photovoltaic cell in his father's lab in 1839 when he was just 19 years old. The first practical solar cell was invented in Bell Laboratories by Calvin Souther Fuller, Daryl Chapin and Gerald Pearson in 1954.

Solar cell basically is a device that converts sunlight into electricity via photovoltaic effect. When photons of sunlight illuminates conducting electrode, it is absorbed by active layer of solar cell generating electron-hole pair is activated. Then carriers move these electron hole couple causing electrical current to flow.

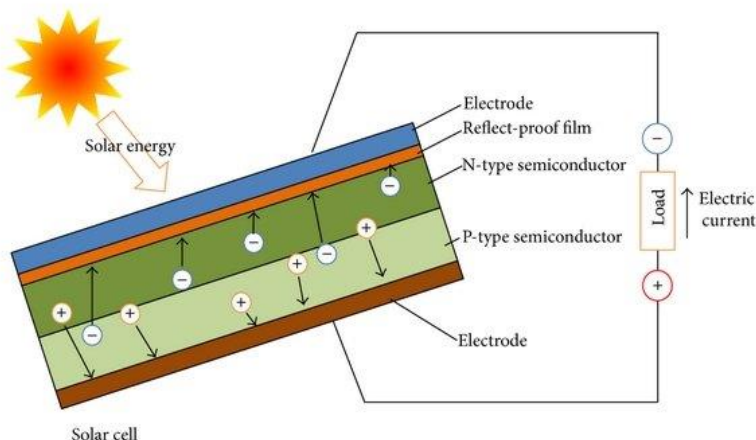


Figure 3.4. Basic working principle of a simple solar cell⁵⁴.

3.2.1. Equivalent Circuit of a Solar Cell

The whole I-V curve of a solar cell, array, or module is represented by equivalent circuit model. The single diode model, which is based on physical principles

and corresponds to the circuit shown below (Figure 3.5) for a single solar cell, is one fundamental equivalent circuit model that is frequently used.

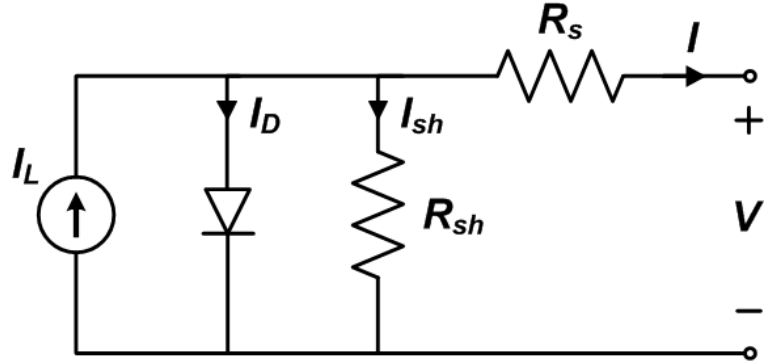


Figure 3.5. The equivalent solar cell circuit model under illumination⁵⁵.

To calculate the current on the junction in A node, Kirchhoff's current law states that

$$I = I_L - I_D - I_{SH} \quad (3.1)$$

Where I_L , I_D and I_{SH} is the photocurrent, diode current, and shunt current of the solar cell respectively.

Since parallel voltages are equal, the voltage across the diode can be defined as:

$$V_D = I_{SH}R_{SH} \quad (3.2)$$

Then, voltage across the diode given as output voltage is

$$V_D = V + IR_S \quad (3.3)$$

Shockley equation in an ideal diode states the diode current as

$$I_D = I_0 \left[\exp \left(\frac{V+IR_S}{nV_T} \right) - 1 \right] \quad (3.4)$$

Where I_0 is the saturation current, n is ideality factor for a diode, R_S is the total series resistance, and V_T is the thermal voltage. For an ideal diode n must be 1, meaning no recombination present along the diode. However, in reality the ideality factor is between 1 and 2.

So, V_T can be express as

$$V_T = \frac{k_B T}{q} \quad (3.5)$$

Here q is the elementary charge, k_B is the Boltzmann constant and T is the temperature. When combined these equations, output current can be express as

$$I = I_L - I_0 \left[\exp \left(\frac{q(V+IR_S)}{k_B T} \right) - 1 \right] - \frac{V+IR_S}{R_{SH}} \quad (3.6)$$

3.2.3. I-V Characteristics of Solar Cell

A specific photovoltaic (PV) cell, module, or array's current and voltage (I-V) characteristics are displayed in the solar cell I-V characteristic curves. It provides a thorough explanation of its capacity and effectiveness for converting solar energy. The output performance and solar efficiency of a solar cell or panel are greatly influenced by its electrical I-V properties, particularly its P_{max} .

The current-voltage (I-V) characteristics of a typical PV cell operating under typical circumstances are displayed in the Figure 3.6. The output current and voltage of a solar cell is responsible how much power they can generate ($I \times V$). Power curve is achieved for a particular radiation level if the multiplication is carried out point for point for all voltages from short-circuit to open-circuit circumstances.

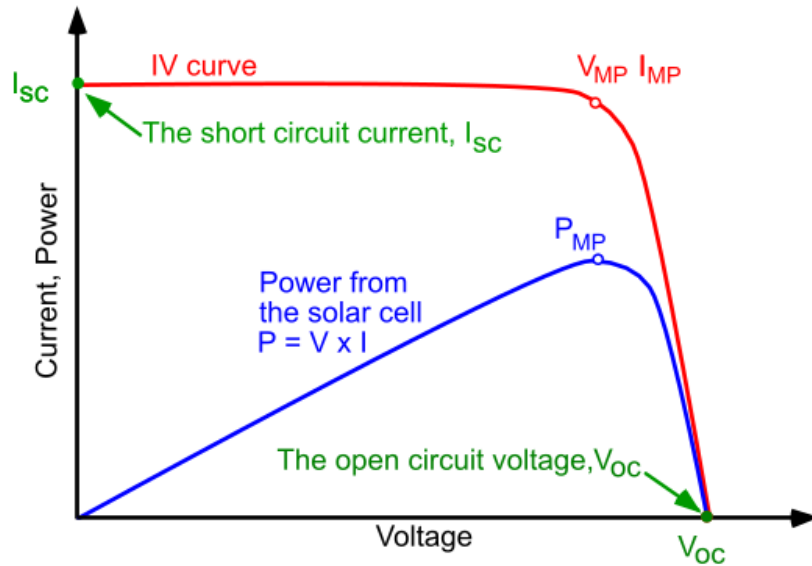


Figure 3.6. Current and voltage (I-V) curve of a solar cell⁵⁶.

When solar cell open-circuited, meaning it is not connected to any load, current will be its minimum (zero) and voltage across the solar cell is at its maximum called open circuit voltage (V_{oc}). On the other hand, the voltage across the solar cell is at its lowest point (zero) when the positive and negative ends are connected together, while the current leaving the cell is at its highest point. This is called as the solar cell short circuit current, or I_{sc} .

Fill factor (FF) is also another crucial parameter to understand the efficiency of PV cells. It is calculated as

$$FF = \frac{P_{max}}{(V_{oc}I_{sc})} \quad (3.7)$$

It measures the actual greatest power that may be achieved. A higher fill factor results in increased efficiency and yielding the cell's output power closer to its theoretical maximum by increasing the shunt resistance (R_{sh}) and decreasing the series resistance (R_s).

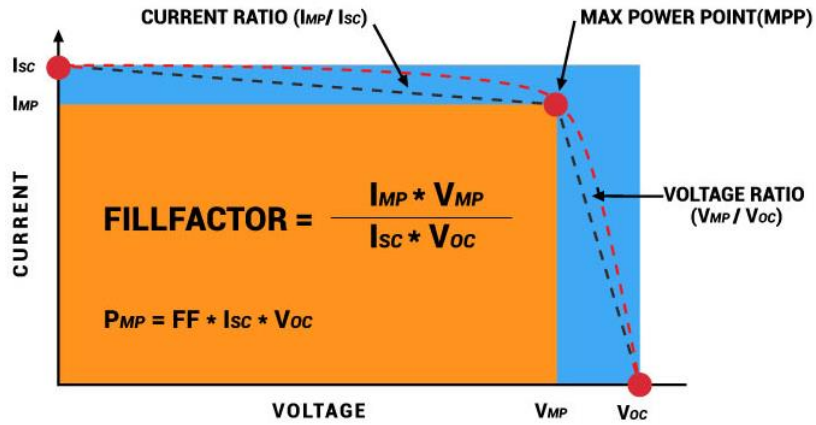


Figure 3.7. Fill factor of solar cell⁵⁷.

3.2.4. Efficiency Measurement of a Solar Cell

The ability of a solar cell to generate power from light is its key feature. The ratio of incident light power to electrical output power is referred to as the power conversion efficiency (PCE) and is defined as

$$\eta = \frac{P_m}{P_{inc}} = \frac{I_m V_m}{P_{inc}} \quad (3.8)$$

Current-voltage (IV) measurements are used to calculate the PCE and other important metrics. The solar cell receives a sequence of voltages while it is illuminated. The typical "IV curve is produced by measuring the output current at each voltage level.

External quantum efficiency (EQE) and internal quantum efficiency (IQE) are another important parameters when investigating solar cells. EQE is the ratio between a number of charge carrier collected by cell with the number of incident photons. IQE is the value of only absorbed photons. Consequently, EQE is always less than the value of IQE.

3.2.5. Shockley-Queisser Limit

The greatest possible solar cell efficiency with a simple single p-n junction was first calculated in 1961 by William Shockley and Hans-Joachim Queisser. The theoretical threshold was estimated to be roughly 33%. Accordingly, a silicon solar cell with a single p-n connection might capture up to 33% of the sun's energy on a sunny day. Of course, there was not enough technology to achieve 33 percent; instead, it was more like 10 percent for a variety of reasons.

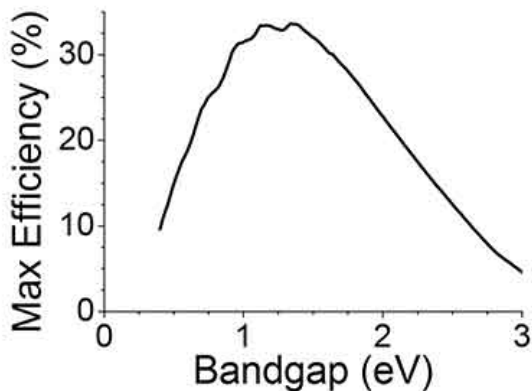


Figure 3.8. Shockley-Queisser limit maximum efficiency of one p-n junction solar cell⁵⁸.

Primary factors responsible for the losses are below band gap and thermalization (hot carrier) losses. Those two reasons combined make up of >55% of the losses. In order to minimize losses, it is important to maintain a proper balance between bandgap energy and photon energy.

Incorporating a low bandgap and a high bandgap semiconductor help to get over this restriction. As a result, this structure (perovskite/silicon tandem) offers multiple benefits to various spectra. Consequently, there is a chance that solar cells' efficiency will rise.

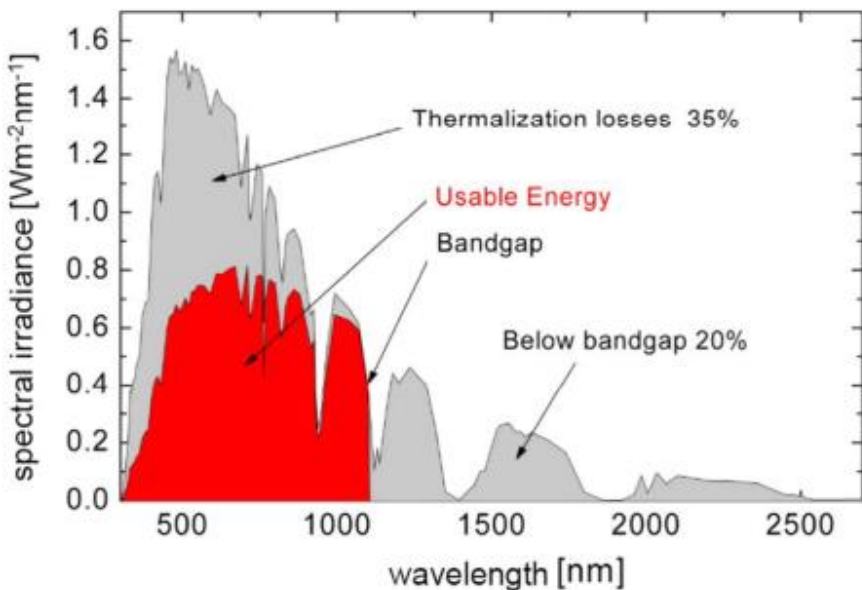


Figure 3.9. Solar spectrum losses of Si solar cell.⁵⁹

3.3. Organic Inorganic Halide Solar Cell

Methyl ammonium lead iodide, $\text{CH}_3\text{NH}_3\text{PbI}_3$ and methyl ammonium lead bromide $\text{CH}_3\text{NH}_3\text{PbBr}_3$ perovskites emerge as a light harvester layer in PV technology. In a solar cell with just over than 3.5% efficiency, hybrid perovskite was first implemented as a light absorber in 2009⁶⁰. Its facile processing, tunable bandgaps, and superior charge-transfer properties make them promising semiconductor in the use of solar cells⁶¹.

3.3.1. Basic Optic Properties

These hybrid halide crystals are ionic crystals exhibiting semiconducting characteristics. The optical absorption wavelength of halide perovskites varies greatly depending on the type and molar ratio of halides (I, Br, Cl) prevalent in the structure, similar to the class of silver halide ionic compounds⁶².

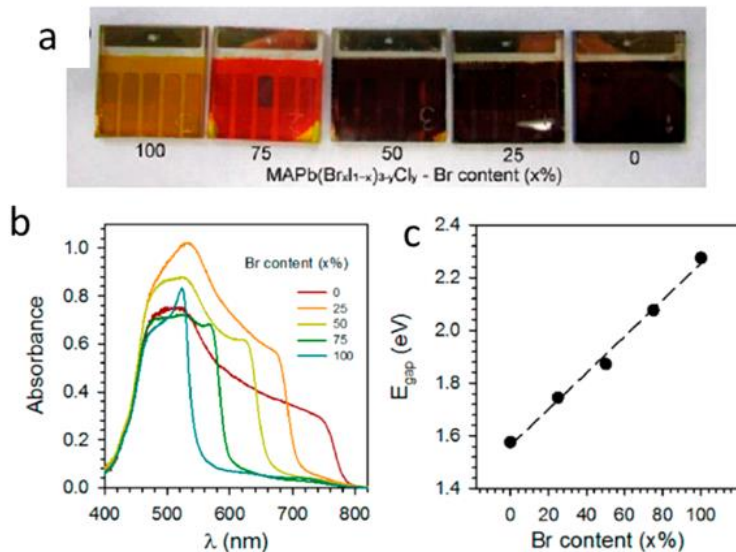


Figure 3.10. Wavelength tuning for MAPb halide perovskite with respect to Br⁶²

Halide perovskites have good optical absorption properties that are beneficial for visible light optoelectronics, as seen by the strong absorption at the edge wavelength and the broad flat absorption at the shorter wavelengths. As a typical perovskite absorber in solar cells, methylammonium (MA) lead halide iodide ($\text{CH}_3\text{NH}_3\text{PbI}_3$, also known as MAPbI_3), an uncommon intrinsic semiconductor that exhibits good mobility of both photogenerated electrons and holes⁶³.

Defect formation has little impact on the photovoltaic capabilities of these perovskites. The high carrier diffusion lengths, measured over the PL lifespan, range from 1 μm (polycrystalline film)⁶⁴ to over 100 μm (single crystal)⁶⁵, reflecting the defect-tolerant character of perovskites.

Moreover, MAPbI_3 exhibits equal effective mass values for both electrons and holes (0.23-0.29)⁶⁶ as an intrinsic semiconductor with ambipolar carrier mobility which is a unique quality that this ionic crystal possesses. Photogenerated carriers in MAPbI_3 act as free carriers and can travel in the perovskite active material for a considerable amount of time without recombination, analogous to inorganic solar cells like Si and GaAs^{64,67,68}.

Additionally, it is acknowledged that the high ionic density in halide perovskites inhibits Coulombic interaction by having a charge-screening impact on the recombination of electrons and holes.

3.3.2. Fabrication and Working Principle

The PSCs operate very much like solid-state p-n junction solar cells. PSCs, as broadly acknowledged currently, operate on the same principles as n-i-p and p-i-n solar cells, with perovskite acting as an intrinsic absorber sandwiched between two selective contacts (p and n).

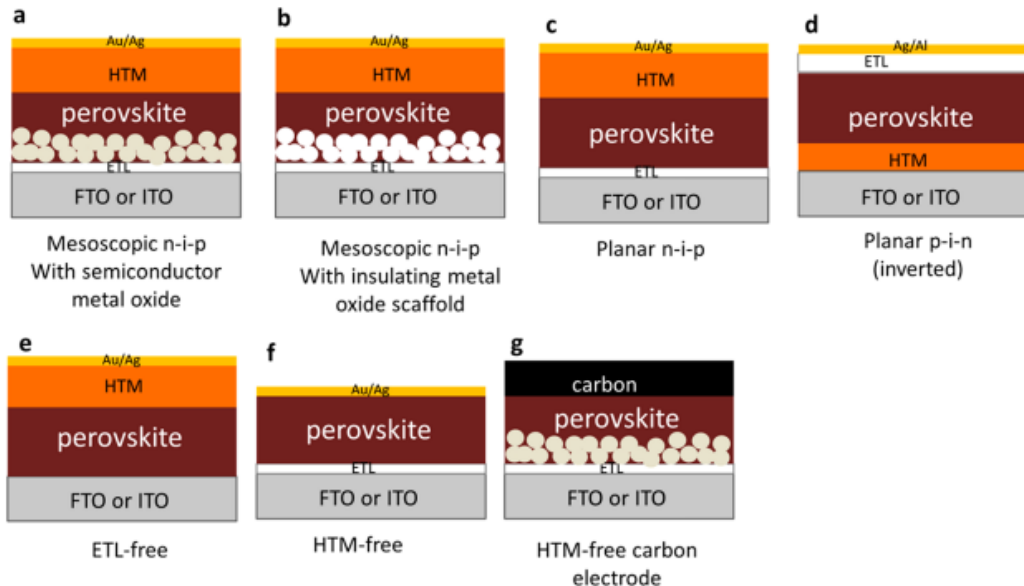


Figure 3.11. Various device architectures of perovskite solar cell⁶⁹.

In the n-i-p structure, TiO_2 (mesoporous or compact) function as an n-type electron transport material (ETM), perovskite acts as the intrinsic (i) absorber, and an organic molecule such as spiro-OMeTAD function as p-type hole transport layer (HTM). Resulting structure is FTO or ITO/TiO₂/perovskite/spiro-OMeTAD/metal contact. An inverted architecture also called p-i-n structure. This time perovskite is sandwiched between p-type layer like PEDOT-PSS at the bottom and n-type material like PCBM at the top. Resulting structure for this configuration is FTO or ITO/ PEDOT-PSS /perovskite/ PCBM /metal contact. Exemplary architecture for some PCs is depicted in Figure 3.11

Light is absorbed by the perovskite, which creates electrons and holes. The n-type ETM layer preferentially collects electrons, while the p-type HTM layer selectively

collects holes. Electrons travel through the external circuit to the p-type layer, where they rejoin with the holes.

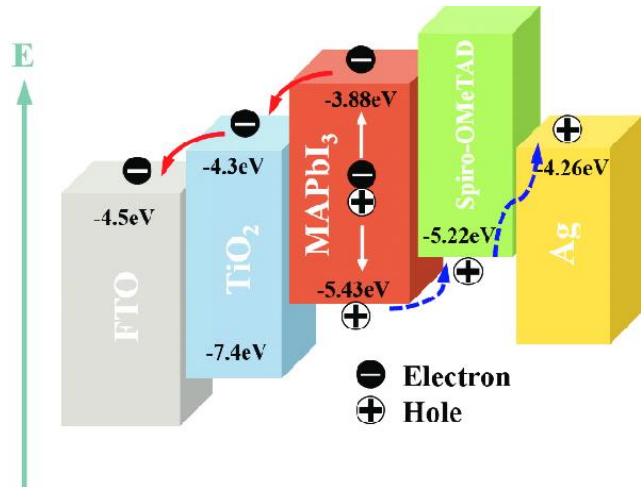


Figure 3.12. Energy diagram for PSC⁷⁰.

The perovskite active layer coated on a compact layer of titanium dioxide (TiO₂) substrate experiences photoexcitation by absorbing wavelength equal to its band gap, then excited state electrons (LUMO) of the perovskite are infused to the conduction band of TiO₂ and migrated through the layer to reach the FTO substrate. After that it travels in an external circuit to the opposite electrode (cathode) where it completes its full cycle with oxidized electrolyte.

The extraordinarily high PCE and high V_{OC} attained with perovskite-based solar cells are widely recognized to be related to the perovskite's remarkably outstanding characteristics such as high absorption coefficient $\alpha > 10^5 \text{ cm}^{-1}$, long carrier lifetime,^{71,72} moderate carrier mobility,^{73,74} slow carrier recombination and high defect tolerance,⁷³ ultralong carrier diffusion length.^{64,75,76}

3.3.3. Crystallization

When a perovskite solution is deposited on the substrate, thermal energy rises as a result of the applied heat, and the perovskite layer begins to nucleate. Nucleation rises with increasing temperature. The nuclei then expand and form crystalline, and the

process is repeated until the material is depleted. The sizes of these crystals have a crucial role in the device's performance. These crystalline grains diameter ranging from 400 to 1500 nanometers in an efficient device, and these crystal grains should be uniformly dispersed across the surface. Large grain sizes have positive affect on the performance of the solar cell^{77,78}. So, grain boundaries are an undesirable property of a crystalline of the solar cell.

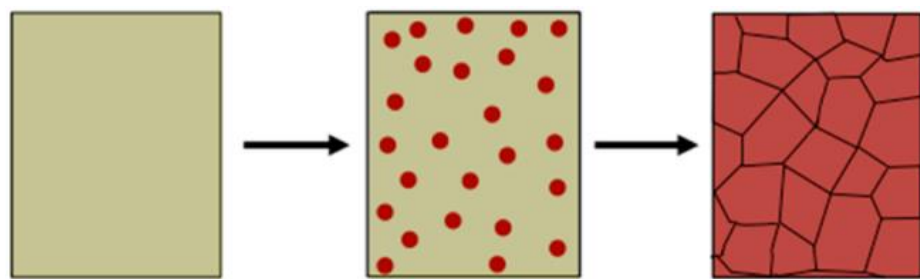


Figure 3.13. Representative process of nucleation and grain growth⁷⁹.

In spin coating technique, before deposition applied, heating the precursor solution, and annealing the substrate is desirable processes. On the other hand, for spray coating technique, it is preferable to heat the substrate and sinter after the deposition. Zhou et al. heated the precursor solution at various temperatures prior to spin coating, then annealed it at 90°C to see how it affected crystal sizes. It was discovered that the highest grain sizes appeared at temperatures ranging from 80 to 85°C, as shown in Figure 3.14⁸⁰.

Sintering after the deposition is a typical operation used in both deposition processes to eliminate solvents from the film and achieve homogeneity. A study on surface morphology and the efficiency of annealing temperature was investigated by a research team. They indicated that the lowest temperature for forming the $\text{CH}_3\text{NH}_3\text{PbI}_3$ perovskite should be 80°C.

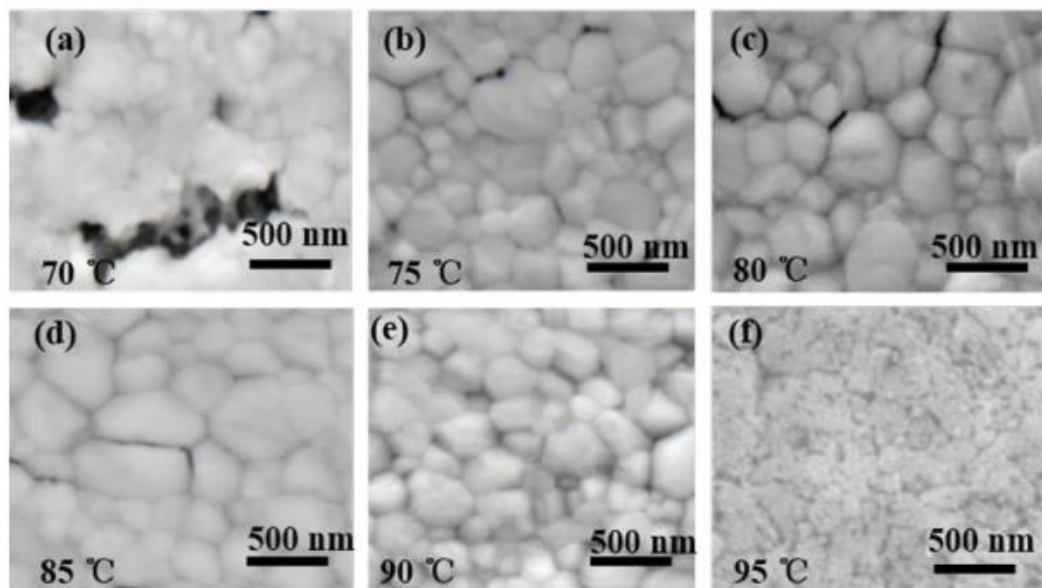


Figure 3.14. Different grain sizes with respect to precursor solution temperature⁸⁰.

3.3.4. Deposition Techniques

Currently, perovskite films are deposited by number of techniques. In this section, we examine conventional techniques as well as the scalable ones.

Spin coating is basically a process of dropping the precursor solution onto a substrate. The substrate then is subsequently spun at a few thousand revolutions per minute by the spin coater (rpm). The solution is distributed equally across the surface, and the spinning eliminates some of the solvents, such as DMF (dimethylformamide). Thickness of the film and is inversely proportional to rotational speed. After that deposited film placed on a hot plate about 100-120 °C for annealing about 10-20 minutes. This process is vital to eliminate the solvent and formation of crystallization. Fabrication with this method causes smooth morphology. This approach has created the most efficient devices up to the present day.

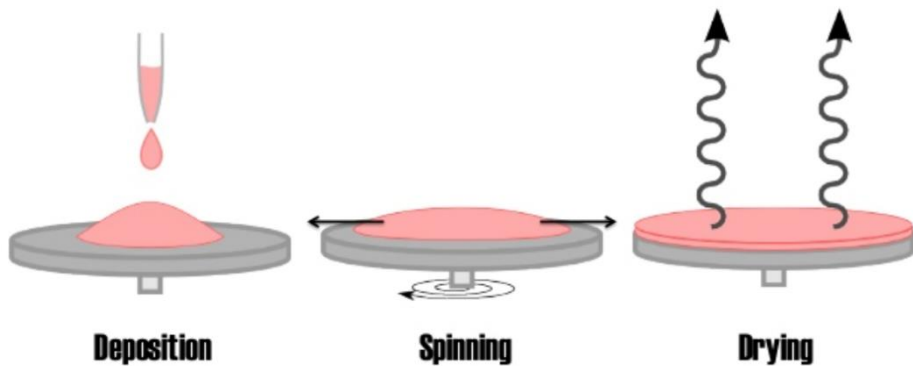


Figure 3.15. Basic spin coating process⁸¹.

However, a significant amount of material is sacrificed during the casting process. As a result, spin coating is neither a scalable, economically viable, or environmentally friendly technology. Furthermore, this approach is not ideal for large-area devices. These drawbacks hinder this technology from being commercialized.

PSC yields from scalable approaches are lower than those obtained via spin-coating. However, recent research has shown that the gap is closing. PSCs must have low production costs in order to be marketed. To reduce production costs, material waste should be minimized. Scalable methods can be used to accomplish this. Scalable approaches include slot-die coating, spray coating, inkjet printing and blade coating.

A blade is used in the blade-coating deposition technique to spread precursor solution across substrates to create wet thin films. Several parameters influence film thickness, including the concentration of the precursor ink, the distance between the blade and the substrate, and the speed at which the blade moves across the substrate. This technology can be extended for continuous fabrication with roll-to-roll setups, in which the blade remains stationary while flexible substrates on a roller move. Ink waste is significantly decreased when compared to spin coating, especially when using continuous roll-to-roll deposition. PSCs made through blade coating have PCEs greater than 19%^{82,83}.

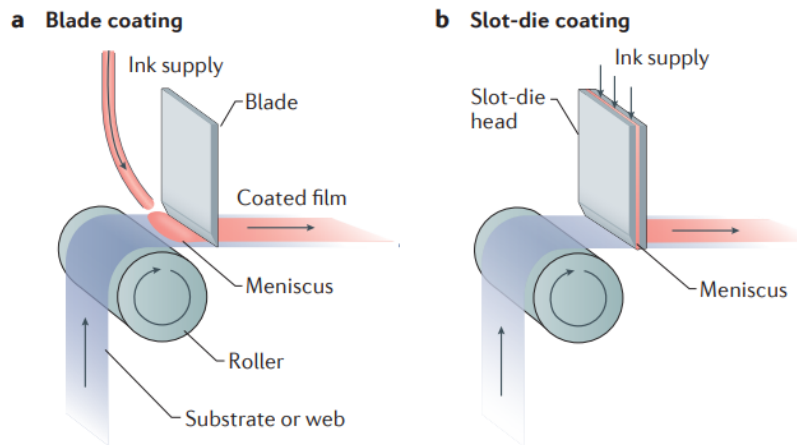


Figure 3.16. Blade and slot-die coating⁸⁴.

Similar to blade coating, slot-die coating in Figure 3.16 employs an ink supply with a tiny slit to transfer ink to the surface. Slot-die coating allows for more precise control of ink flow, but it typically needs more ink to fill the ink reservoir and supply pipe, making it less useful for the creation of novel ink chemistries. Due to the lack of research into slot-die coating, the PSCs produced today have a far lower PCE than those made through blade coating.

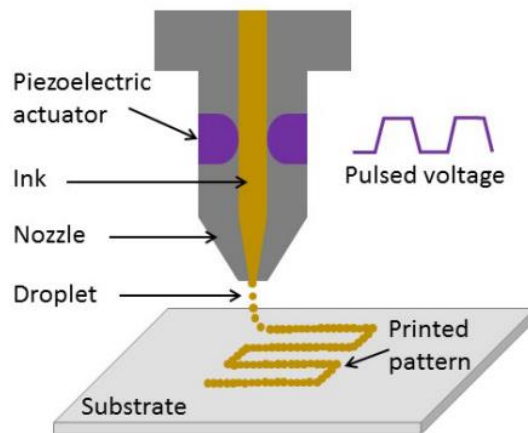


Figure 3.17. Inkjet printing technique⁸⁵.

Nozzles are employed in inkjet printing to disseminate the precursor ink, allowing for precise control over the droplet size and direction as illustrated in Figure 3.17. As shown by digital printers, ultrafine lateral resolution is made possible by miniature nozzles and a close proximity between the nozzles and substrate. Electronics

can be printed using this patterning capability. Inkjet printing has been used to create PSCs with small areas (0.04 cm^2). Nevertheless, the printing rate and device design will determine whether inkjet printing is appropriate for the high-volume, large-area manufacturing of perovskite solar modules.

One of the most commonly used method in solar cell industry is screen printing. Cell precursors with a frontside emitter and anti-reflection coating are loaded into a cassette for processing. Printing tool consist of a mesh screen with a selective openings which can form either a grid or full area contact.

The rear side of each precursor paste is printed onto the full area to form the back contact. During the printing process a squeegee is used for spaced through the screen mesh and a flood bar is used to replenish the paste after each print.

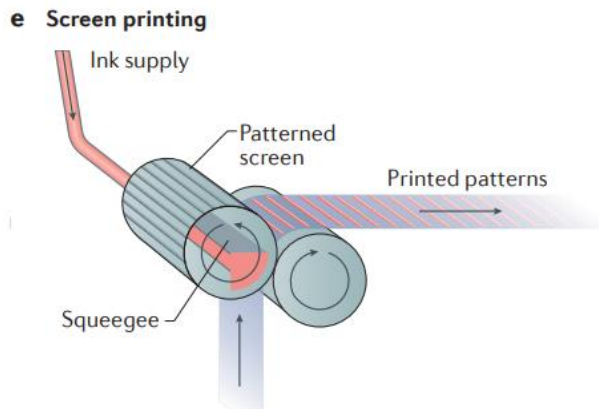


Figure 3.18. Screen printing⁸⁴.

Other important scalable deposition technique is spray coating. Since it is the main deposition technique used in this thesis it will be analyzed in the next section in detail.

3.3.5. Spray Coating

Nowadays, spin coating, which includes spreading the perovskite precursor solution across a substrate using shear pressures, is used in the majority of studies to develop perovskite materials. The majority of high-efficiency devices documented in

the literature were created using this method since it is straightforward and widely available. Nevertheless, low process consistency amongst research laboratories can be a problem for spin coating. Due to the wasted solution that is lost from the substrate during coating and the usual introduction of thickness nonuniformities when increasing the coated area beyond a few square centimeters, it is therefore not well suited to coating large regions⁸⁶.

Spray deposition on the other hand is using a nozzle to disperse precursor droplet onto substrate. Spray coating technique can be categorized as the way it generates droplets such as pneumatic spraying, ultrasonic spraying or electrospraying.

In the process of spraying, droplet size and position are arbitrary, and numerous droplets must intersect in a small region to guarantee complete coverage.

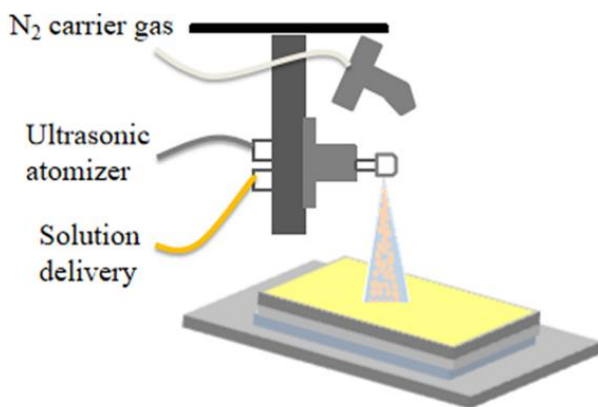


Figure 3.19. Illustration of spray-coating procedure⁸⁶.

Barrows et al. used the $\text{CH}_3\text{NH}_3\text{PbI}_{(3-x)}\text{Cl}_x$ perovskite solution under environmental temperature to carry out one of the earliest studies on spray-cast perovskite solar cells. They architected ITO/PEDOT:PSS/Perovskite/PCBM/Ca/Al device structure and accomplished over 11% PCE⁸⁷.

By spray-coating the HTL, ETL, and absorber layer $\text{CH}_3\text{NH}_3\text{PbI}_{(3-x)}\text{Cl}_x$ in ambient conditions, Mohamad et al. achieved 9.9 percent efficiency with an inverted architecture. They applied spin-coating to these layers while using the same materials and a nitrogen environment to cover them. In this case, their efficiency was 12.8%.

They attributed the drop in yield from the spray to uniformity and insufficient surface covering.

There are several attempts to increase the efficiency of the perovskite film by applying two step deposition. Huang et al. engineered to create uniform, smooth, and centimeter-scale perovskite $\text{CH}_3\text{NH}_3\text{PbI}_3$ films for effective, large-area solar cells, a two-step ultrasonic spray technique has been devised. Perovskite films made using this technique demonstrated improved crystallinity, lower non-radiative recombination, and more effective interfacial charge extraction capabilities, in addition to advantages in larger area and higher smoothness. A mesoscopic solar cell with an efficiency of 16.03 % was ultimately developed through methodical refinements. Additionally, a large-area ($1 \times 1 \text{ cm}^2$) cell with a 13.09% efficiency was also created. In order to deposit high-quality and wide-area perovskite absorbers and provide excellent cell performance, this work shows that the two-step spray approach can be a feasible alternative⁸⁸.

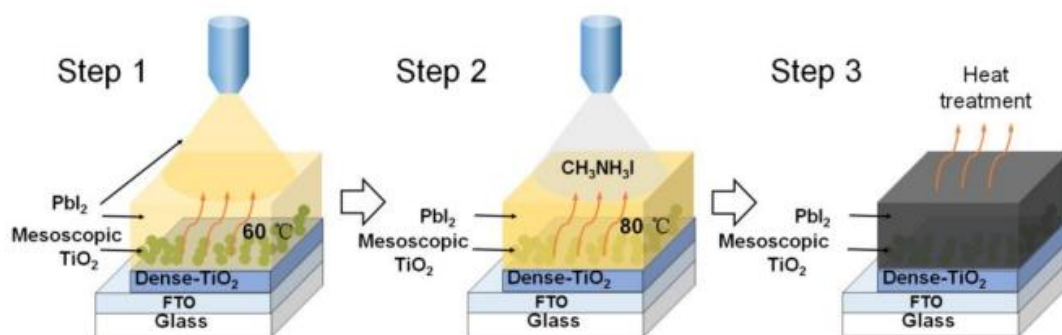


Figure 3.20. Illustration of two step ultrasonic spray⁸⁸.

As of now, the greatest recorded power coefficient efficiency by using spray coating technique is over 20%⁸⁹. In this study they examined how chlorine-containing (Cl) perovskite inks may be applied to a large processing frame for spray-coated PSCs in atmospheric circumstances. It was shown the ink they use can be employed with scalable deposition techniques of spray coating because of its outstanding adaptability and transferability. They were able to create reproducible with pinhole-free films via gas-assisted method.

Crystalline grain growth is a crucial parameter affecting the morphology and consequently PCE of the perovskite film. By altering a few spray-coating parameters, it

is possible to enhance crystalline grain development, which is one of the elements determining the device's performance.

Heo et al. proposed a mechanism for the crystalline grain growth of the perovskite $\text{CH}_3\text{NH}_3\text{PbI}_{(3-x)}\text{Cl}_x$ ⁹⁰. They represented that spraying $\text{MAPbI}_{(3-x)}\text{Cl}_x$ precursor solution onto hot FTO/TiO₂ as inward flux (F_{in}) of the precursor solution outward flux (F_{out}) of the solvents and the experimental settings allow for adjustment of the F_{in}/F_{out} ratio.

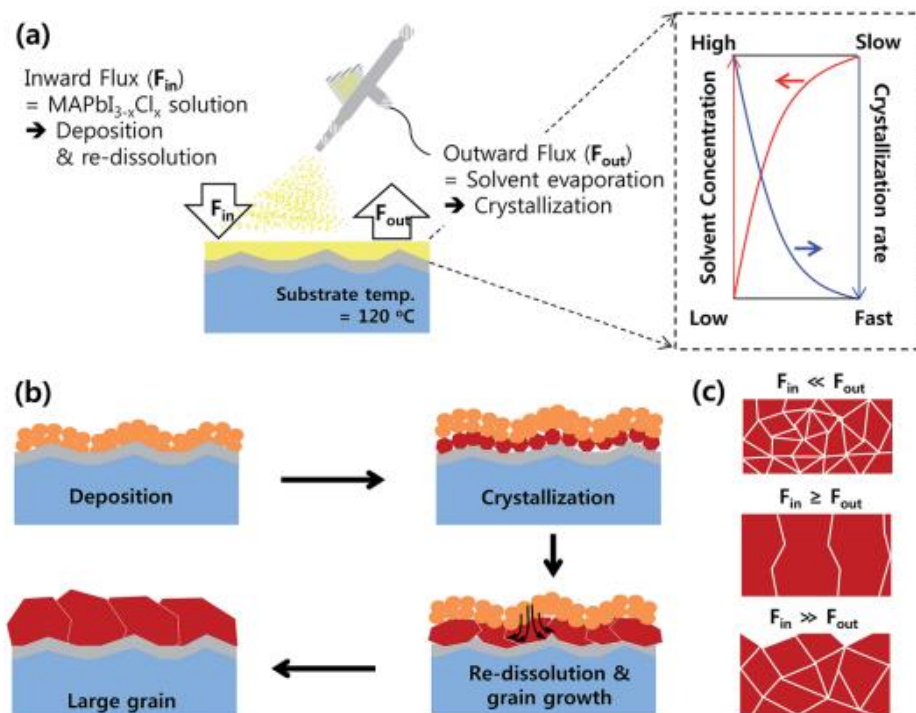


Figure 3.21. Schematic illustration mechanism for the spray-coating process⁹⁰.

DMF and DMSO are typical solvents in perovskite solutions. DMF is a solvent that evaporates rapidly and does not fall into the hot plate during spraying. DMSO, on the other hand, is a gradually evaporating solvent that vaporizes off the film when it encounters a heated substrate. In this regard, DMSO has a delayed crystallization impact, which is used to restore the equilibrium between F_{in} and F_{out} .

When F_{in} is significantly smaller than F_{out} film crystallizes rapidly causing small crystalline grains thus light harvester layer does not perform well.

When F_{in} is significantly greater than F_{out} , the initial droplets combine with successive drops as they reach the substrate before crystallization starts. The obtained wet perovskite film is required the heat treatment. A rough surface and small grain on the film are merged.

When $F_{in} \geq F_{out}$ or another word F_{in} is comparable or hardly greater than F_{out} sprayed droplets can re-dissolve and creating grain growth which is desirable process due to the fact that the larger grain sizes have positive affect on the performance of the solar cell.

CHAPTER 4

EXPERIMENTAL METHODOLOGY

In this section, our spray deposition system and lab-scale perovskite solar cell perovskite fabrication is explained in detail which involves every step of the processes.

4.1. Novel Spray Deposition System

As seen in Figure 4.1 displays spray nozzle for our spraying system to cast perovskites.



Figure 4.1. Spraying nozzle

This nozzle is the one that mostly used head in our experiments. It has three out gas flow with two blowing hot nitrogen gas and one is for solution. It gives the ability to cast the deposition in a rectangular-like shape area.

Top and side view of the sprayed head is depicted in Figure 4.2. Respective input gas flows, angles between them, diameter, and distance between apparatuses are shown.

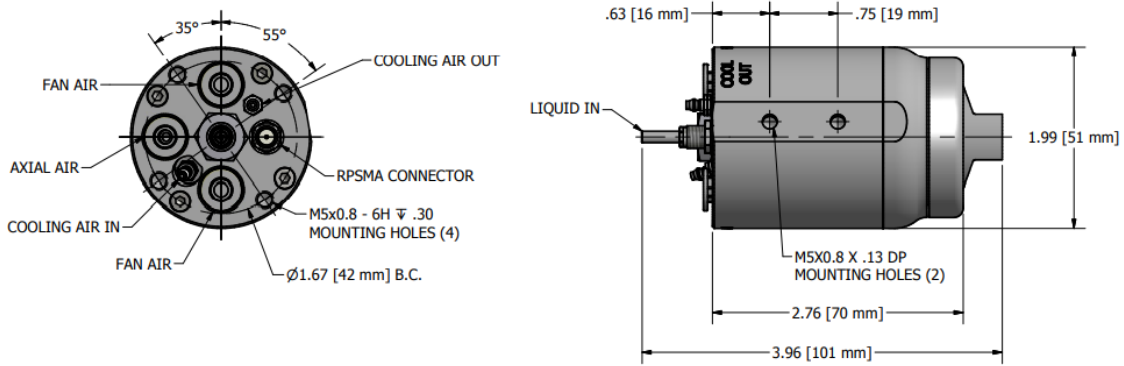


Figure 4.2. Top and side view illustration of the nozzle.

As shown in Figure 4.3 there are also two important mechanisms when we conduct our experiments. Figure 4.3a is hot nitrogen gas carrier pipe, gas temperature that it blows is controlled by a PID controller. In Figure 4.3b, nozzle placed in a metal plate with two ends and this bloc is connected with a four-wheel rectangular apparatus. This is the whole system above the metal rods with slits. This whole system is moving via plastic straps that is screwed to metal platform consisting of metal rods with slits.

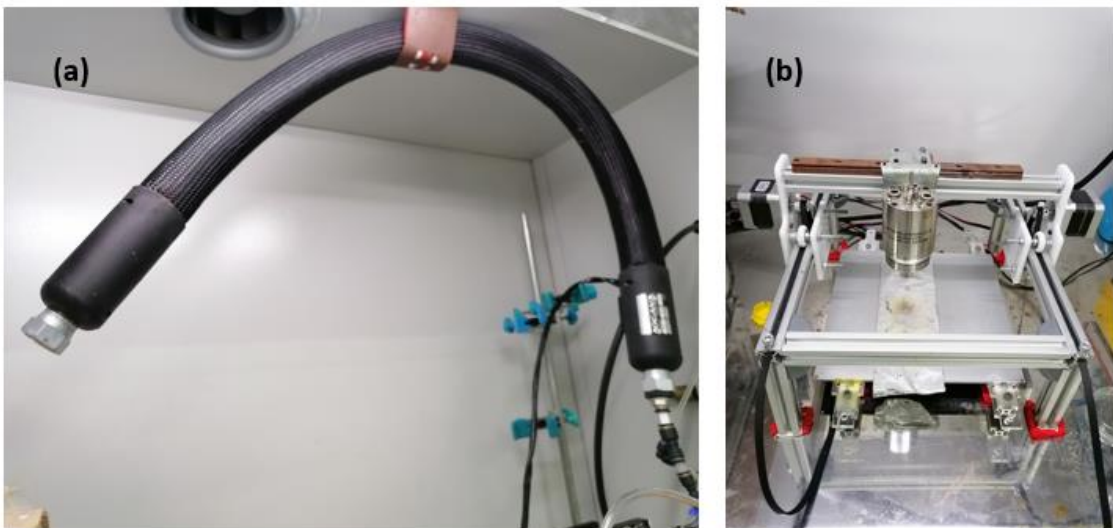


Figure 4.3. (a) Hot N₂ gas carrier, (b) dynamic spray system

The basic working principle of our system can be summarized as follows. Dynamic nozzle system is moved on the y-plane with the help of a two step motors. Speed and position of the nozzle is controlled by a microcontroller which is also

connected to a computer. Spraying nozzle's power is obtained by ultrasonic generator. This ultrasonic generator capable of generating high frequencies is responsible to make nozzle to operate at high frequency, and nozzle therefore could break the precursor solution into its droplets (i.e. ultrasonic atomization). In order to prevent the nozzle from overheating, small flexible plastic pipe connected to the compressor is used to deliver the air to the nozzle.

Syringe pump is used to deliver the solution to nozzle and also adjust the pumping rate of the precursor solution. Nitrogen gases coming to the nozzle and hot gas carrier pipe are supplied by nitrogen cylinders with a required pressure rates. All gas pressures are measured and controlled by manometers. Our resulting novel spray deposition system is shown in Figure 4.4.

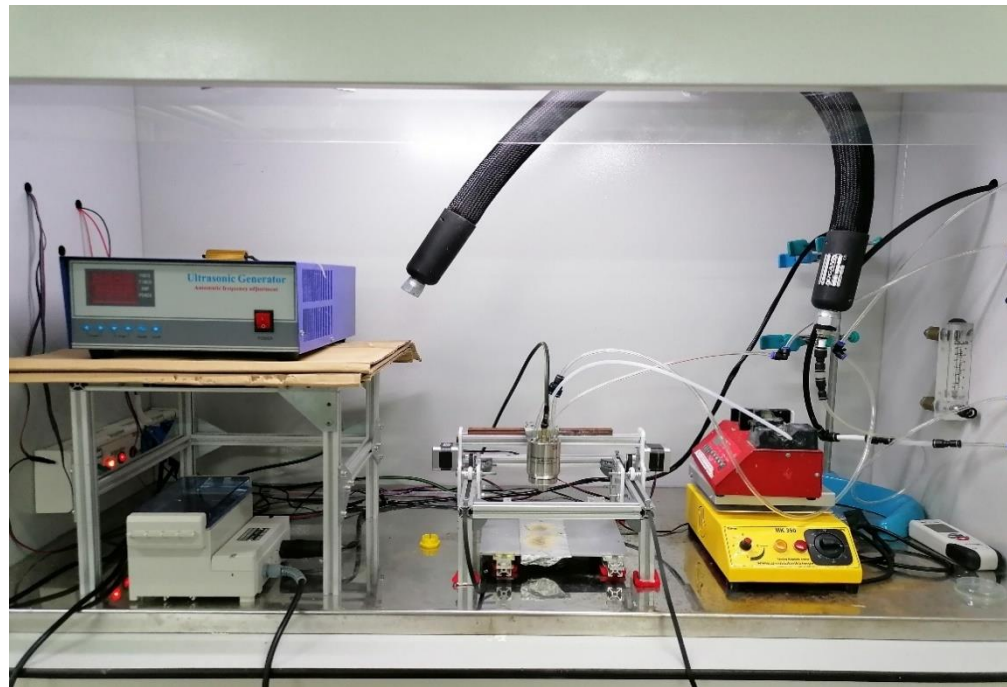


Figure 4.4. The complete system of the spray cast deposition.

4.2. Perovskite Solar Cell Fabrication

4.2.1. Etching

Etching is a technique for removing material from a substrate. To electrically characterize and work PCE properly, etching is used to obtain anode and cathode layer. Physical, chemical, wet, dry, and isotropic or anisotropic etching methods are all possible. When manufacturing solar cells, any of these etch process modifications can be applied.

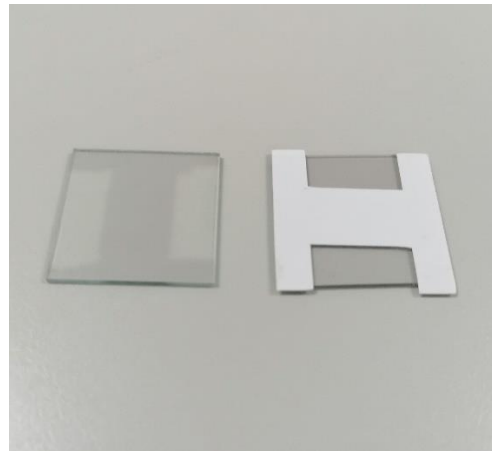


Figure 4.5. Etching process.

Tape is used to mask the areas that is not wanted to be etched. Then the areas to be etched is sprinkled with zinc powder, and dilute HCl (hydrochloric acid) droplets are dripped to dissolve and remove the zinc powder of the surface of the FTO coated glass. Zinc electrons have a negative charge on the FTO surface, which makes H_3O^+ ions want to stick around. Tin oxide is exposed to hydrogen ions, which dissociate them from one another. FTO coated glass is etched as a result of this. A cotton swab dipped in deionized water is used to clean etched FTOs before drying with N_2 gas.

4.2.2. Cleaning

Etched substrates are cleaned for 10 minutes each in detergent water, deionized water, and isopropanol respectively. Each sample is dried with N₂ gun. Then all samples are put into oxygen plasma cleaner to eliminate organic compounds from the surface (10-2 mbar, 70 W) for 8 minutes.

4.2.3. Electron Transport Layer

Titanium diisopropoxide bis (acetylacetone) (TiDIP) and ethanol are mixed in a 1:9 ratio to create the c-TiO₂ solution. The titanic paste is diluted in 22 percent weight of ethanol to create the m-TiO₂ solution.

On the well cleaned substrates, ETL is spin coated by using micropipette. It is important to note that it must be a two-step process, when coating mesoporous layer. The c-TiO₂ layer is first created by dropping TiDIP solution onto the substrates in the spin coater and rotating them for 30 seconds at 3000 rpm. A cotton swab dipped in ethanol, the solvent of the TiDIP solution, is used to clean the two corners of the etched region of the coated substrate. Then the substrate is annealed at 500°C for 30 minutes

Again, by using the spin coater, the m-TiO₂ layer is coated on top of coated and annealed c-TiO₂. The solution of mesoporous TiO₂ is casted with the help of micropipette and spins at 2000 rpm 20 seconds. Two edges of the substrate are cleaned by cotton swab dipped in its solvent of ethanol. Then each cleaned substrate is annealed at 550°C for 20 minutes.

4.2.4. Perovskite Layer

The perovskite precursor solution is obtained by mixing 135.15 mg/ml MAI, 391.85 mg/ml PbI₂, 16.8 mg/ml MABr, 55.05 mg/ml PbBr₂ in DMF:DMSO (4:1) at 50°C overnight. When preparing solution, first lead-free powders is dissolved and react

in DMF:DMSO after that lead containing compounds are added to obtain the best stoichiometry.

MAPbI_{8.5}Br_{1.5} precursor solution is spray casted onto surface having FTO/ c-TiO₂/ m-TiO₂ architecture. The hot plate located beneath the spraying nozzle is ranging from 70-110°C. DMF is quickly removed from the surface when droplets casted on substrate. The resulting film is dried between 10 seconds to 60 seconds depending upon the two basic factors one of which is the temperature of hot plate itself and the other is pipe that is carrying hot nitrogen gas. After that film is placed to anneal at temperatures 100°C. Finally resulting perovskite coated film is wiped by DMF and hold at 60°C each to get rid of the DMF that is used in wiping processes.

4.2.5. Hole Transport Layer

The recipe we use for preparing and coating HTL is as follows. 72.3 mg of Spiro-OMeTAD is dissolved in 1 milliliter of chlorobenzene (CBN) and doped with 17.5 microliters of Li-TFSI solution and 28.8 microliters of tributyl phosphate (TBP). Li-TFSI solution is prepared by mixing 520 milligram Li salt (bis(trifluoromethanesulfonly)imide) per 1 milliliter acetonitrile (ACN). The resulting Spiro-OMeTAD solution is then coated by spin coater in the glovebox. After the deposition the edges of each HTL coated sample is wiped by chlorobenzene and place each sample to desiccator for 24 hours.

4.2.6. Gold Contact

Thermal evaporation is used to coat the samples with gold. The shadow mask is used to put the substrates on the substrate holder. In the vacuum chamber, the sample holder is placed on a rotating plate, and gold is added to a Tungsten boat until the desired thickness is reached.

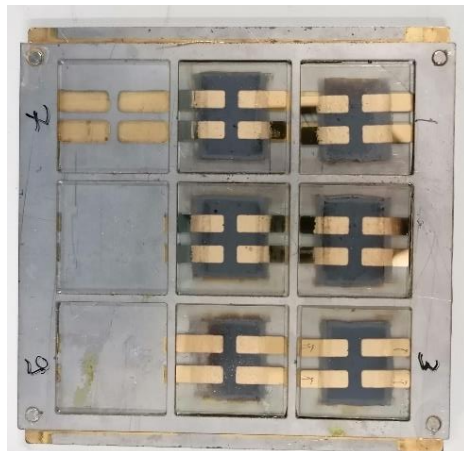


Figure 4.6. $\text{CH}_3\text{NH}_3\text{PbI}_x\text{Br}_{1-x}$ solar cells.

For optimal metal deposition, the chamber is then evacuated by using a rough vacuum pump and a turbomolecular vacuum. The DC power is turned on to heat the tungsten boat until the gold within melts at a pressure of less than $4*10^{-6}$ mbar. The gold begins to evaporate onto the samples due to fact that chamber is conserve its high vacuum. We monitor the rate of gold evaporation with the help of a quartz crystal microbalance apparatus and halt evaporation at the desired ultimate thickness. At least 50 nm of gold should be present. As a result of this process we obtain 4 device on each sample as seen in Figure 4.6.

4.3. Characterization

The procedures for determining the characteristics of perovskite thin films and perovskite solar cells are described in this section of Chapter 4. Chapter 5 will explain the outcomes of these techniques.

4.3.1. Optical Microscopy

An optical microscope is a tool that enlarges images of objects by utilizing lenses. It accomplishes this using visible light. In our experiments, it was used

to swiftly find significant defects and imperfections in films. We can quickly determine whether the film surface is homogeneous using the optical microscope.

4.3.2. Scanning Electron Microscope

Scanning electron microscope (SEM) is a microscope that produce images using electrons instead of visible light. The wavelength of light limits the resolution in an optical microscope. So by using electrons which have a much shorter wavelength than the visible light SEM can create much high-resolution image.

When electrons coming out of electron gun called primary electrons came into contact with sample, they cause atoms of the surface of the sample to emit electrons. These emitted electrons are called secondary electron, and these are what SEMs use to visualize their sample.

Electron beam sweeps or scans the surface of the sample, which causes to discharge secondary electrons. There are two types of detectors in the sample chamber, the secondary electron chamber, the secondary electron detector and backscatter electron detector. The backscatter electron detectors pick up backscatter electrons that come from deeper regions of the sample that are a result of elastic interactions between the beam and the sample. The results from this detector are primarily used to examine crystallography, and the magnetic field of the sample. As a result, we have been able to analyze more about the film's homogeneity and crystal formation. Philips XL 30S FEG is used in our analysis to obtain the information about surface morphology and roughness.

4.3.3. X-Ray Diffraction

In an X-Ray diffraction analysis (XRD), a sample is placed into the center of an instrument and illuminated with the beam of X-rays. The X-ray tube and detector move in a synchronized motion. The signal coming from the sample is recorded and graphed, where peaks are observed related to the atomic structure of the sample, chemical bonds

between them, and crystallographic imperfections. Philips X’Pert Pro X-Ray Diffractometer was used for characterization.

4.3.4. Current-Voltage Measurement

Assembled devices are attached between a printed circuit board (PCB) with embedded pogo pins and a respectively designed slot in order to measure the current-voltage graph (accordance with our shadow mask design).

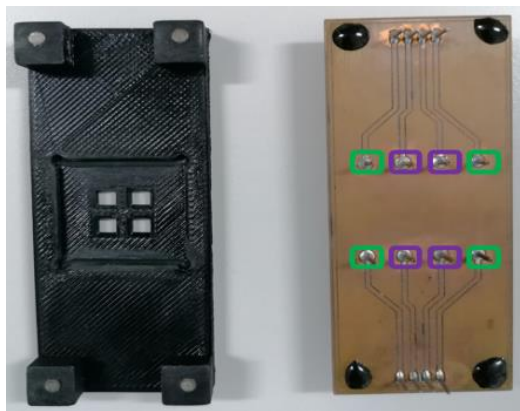


Figure 4.7. Slot and PCB. Purple and yellow boxes touching gold and FTO respectively.

This slot, which has four spots with an area of 0.16 cm^2 , also serves as a shadow mask. The squares on the sample are located precisely below the 4 devices. The cathode is connected to the pogo pin that touches the FTO, while the anode is connected to the pogo pin that touches the gold.

The devices are then exposed to AM 1.5 (1000 W/m^2) illumination using an Abet 11002 SunLite solar simulator, resulting in the creation of 4 active regions in a sample of 0.16 cm^2 . A Keithley 2400 source meter, seen in Figure 4.8, is used to obtain current-voltage curves. Measurements are made in the dark to see if the device performs like a regular p-n junction. Then from 200 mV to 800 mV is applied.



Figure 4.8. Abet 11002 SunLite solar simulator and Keithley 2400 source meter.

CHAPTER 5

RESULTS AND DISCUSSION

5.1. Morphology of Perovskite Thin Films

The most challenging step in this endeavor has been obtaining a homogenous film. Throughout our experiments our main focus was to accomplish pin-hole free, less bush containing, smooth surface roughness, and reduced heterogeneity perovskite thin films. During our experiments, several important factors affecting solar cell morphology and film growth have been observed. In this section we try to explain some of these observations.

Firstly, during spray deposition, film growth processes at initial moments depend on the two basic factors one of which is the temperature of hot plate itself and the other is the pipe that is carrying hot nitrogen gas. The higher the temperature of the hot plate, the higher the rate of removal of DMF solvent from the film, causing fast crystallization. Generally speaking, hot plate beneath the spraying nozzle must be about 80-85°C. Below these temperatures we certainly concluded that film undergoes slow crystallization and slow crystallization causes pin holes, bush-like formations, poor nucleation and inhomogeneous surface.

Quick examination of the morphology of the perovskite films is done by optical microscope. Figure 5.1 shows the certain area of the film exhibiting surface morphology of the perovskite film. Figure 5.1 shows that the under illuminating from both bottom and up indicates the surface morphology of the selected area of the cell is good in optical microscopy regime however pinhole emerges at the bottom of the image.

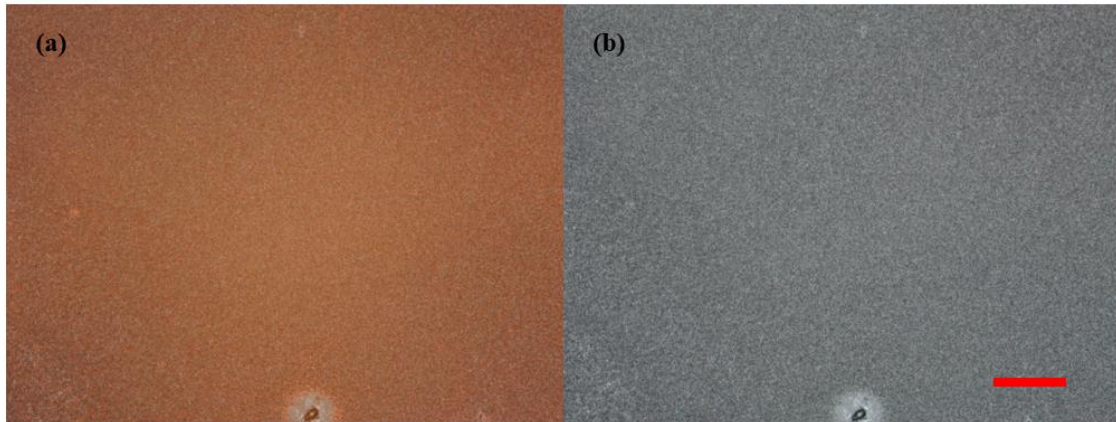


Figure 5.1. Optical microscopy images of perovskite film under illumination from (a) bottom, (b) up, scalebar represents 200 μm

There are other factors impacting the morphology of the perovskite film apart from initial factors of hot plate and hot N₂ blowing pipe. For good crystallization of the film spraying nozzle is placed 4-5 cm above the sample. This distance between the spraying nozzle and sample is the inference of multiple experiments, and the literature works.

Other important parameter in the spray cast deposition is the thickness. Pumping rate of the precursor solution and the speed of the step motor. If the speed of the step motors are increased, then film thickness is decreased and vice versa. That means speed of the motor is inversely proportional to the thickness of the perovskite film. On the other hand if the pumping rate is decreased, then film thickness is decreased and again vice versa. This finding also means the rate of the pumping of precursor solution is proportional to the thickness of the perovskite film. It is important to note that the pumping rate and the speed of the step motor are interrelated factors. For instance decreasing the speed of the motor and increasing the pumping rate has the similar effect on the thickness.

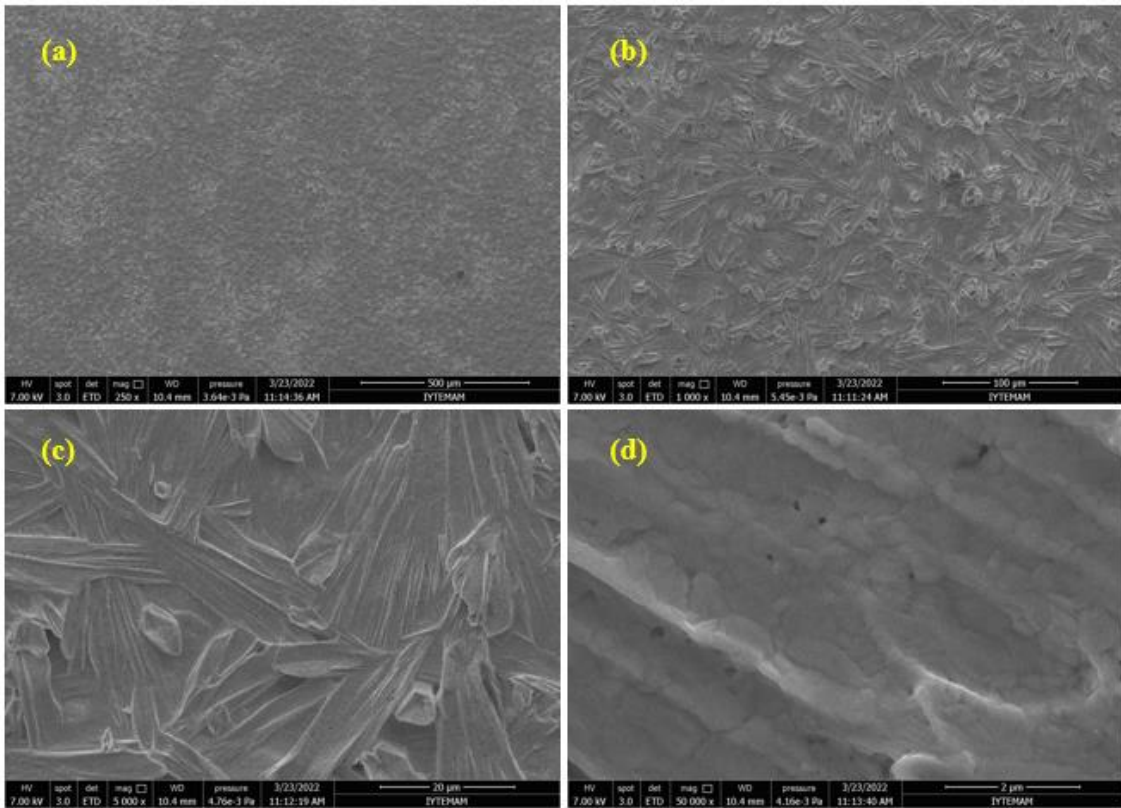


Figure 5.2. SEM images of perovskite films with different distances

Surface morphology of perovskite films at different distances is shown in Figure 5.2. SEM images of perovskite films distanced of (a) 500 μm , (b) 100 μm , (c) 20 μm , and (d) 2 μm . These images indicate that although film has needle like formation on the certain surfaces. Effect of these formations on the perovskite solar cell performances are needed to be further examined.

5.2. Precursor Solution

When preparing the perovskite precursor solution, two kinds of solvents namely DMF and DMSO are mixed in a specified ratio. DMF and DMSO has a boiling point of 153°C and 189°C respectively. Since DMF has lower boiling point compared to DMSO it is the first one to evaporate during the deposition process, most of it is removed from film until they are placed to another hot plate for annealing process.

In this thesis one of our main motivation to observe the effect of respective ratios of DMF and DMSO on the surface morphology and roughness of the perovskite

thin films. Although we keep the DMF 4:1 DMSO volume ratio the same and changed other parameters, we observed that the same needle-like formation and most importantly the high surface roughness repeatedly. We decided to adjust the ratio of DMF and DMSO by half, making 2:1 to see whether this arrangement is capable of fixing these obstacles.

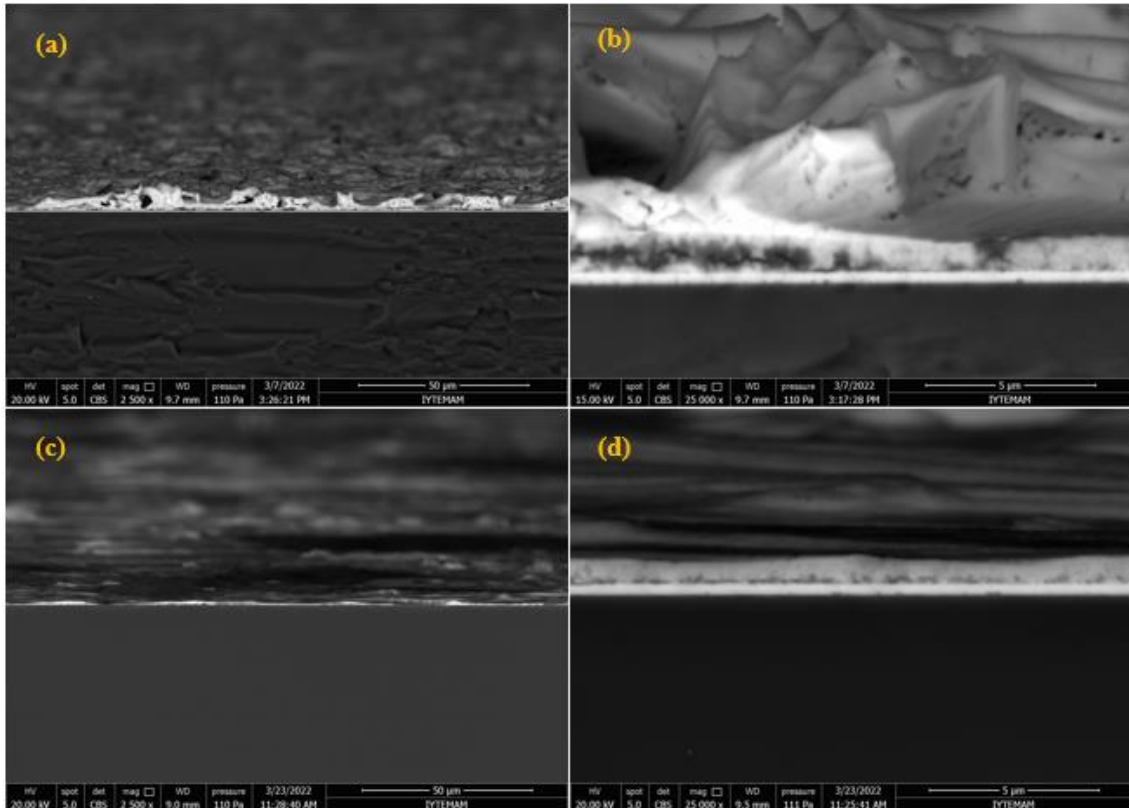


Figure 5.3. Cross-section SEM images

As seen from the Figure 5.3 of (a) and (b) with DMF 4:1 DMSO ratio 50 μm and 5 μm respectively, (c) and (d) with DMF 2:1 DMSO ratio 50 μm and 5 μm respectively. By adjusting the DMF and DMSO ratio we are able to accomplish to lower the roughness of the film. In Figure 5.3c and 5.3d clearly show that the films with less DMF solvent have smooth surfaces then the ones with higher DMF (Figure 5.3a and Figure 5.3b).

However, this approach has number of drawbacks. The main one is that the surface smoothness and grain size of the perovskite film has trade-off relation. Surface roughness decreases with decreasing the size of perovskite grain, causing to a lower

surface recombination. At the same time these smooth films having small grain size lack of short diffusion length and carrier lifetime⁹¹.

All possible electrical connections of magnetic slots consisting of 4 anodes and 4 cathodes are examined to obtain the I-V curves. Since a solar cell is a device that have diode characteristic, we are able to obtain this diode characteristic, although we are not able to achieve desired power conversion efficiency.

In our experiments, perovskite precursor solution has been deposited in a single step onto the surface of FTO/ c-TiO₂/ m-TiO₂ architecture so substantial morphological changes brought on by the uncontrolled precipitation of the perovskite hinder the photovoltaic performance in the final devices.

5.3. Crystallization and Electrical Characteristic of Perovskite Films

It is important to point out that hot N₂ blowing pipe is vital role in our film growth process. Our main motivation of the usage of the N₂ blowing pipe is to mimic the enclosed vacuum space around the solar cell to enhance the homogeneity and, similar to the hot plate, to eliminate the solvent of the wet film.

The higher the temperature of the N₂ blowing pipe, the higher the rate of removal of DMF solvent from the film. Temperature of N₂ blowing pipe is adjusted to 120-140°C to meet the best nucleation of the perovskite film. We concluded that the main function of using the pipe is that the multiple and fast begin of the nucleation process of the film. Decreasing the temperature of the pipe causes mainly poor nucleation which means resulting film have defective morphology.

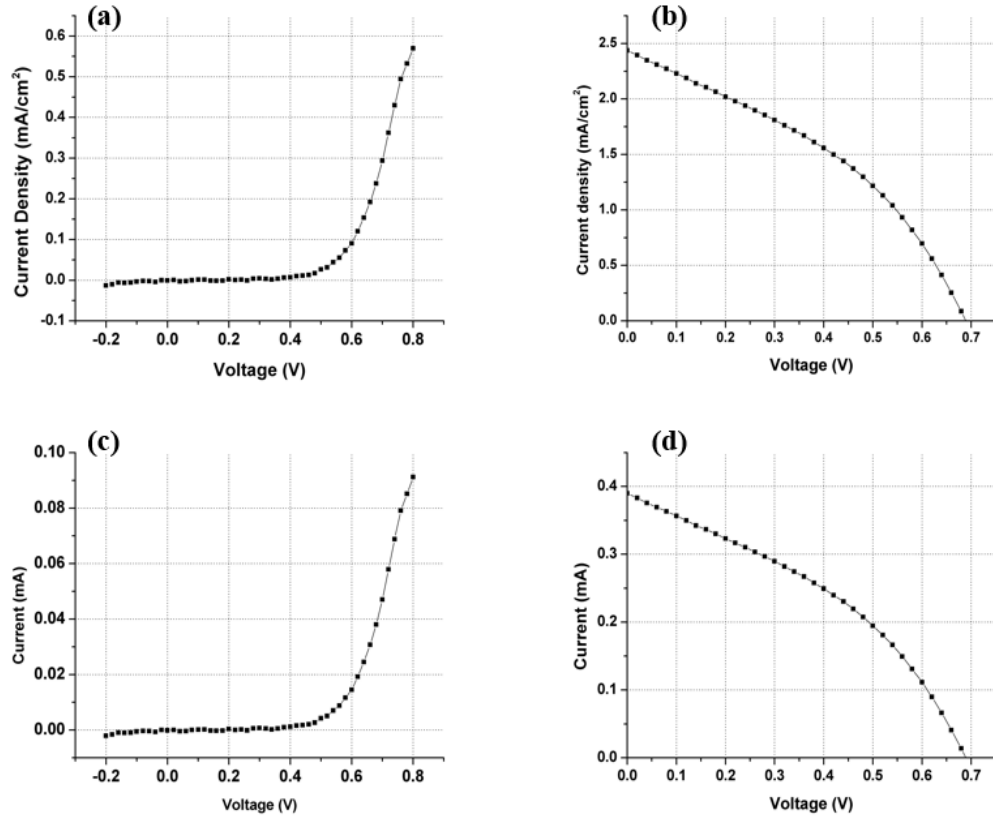


Figure 5.4. (a) and (b) dark and illuminated J-V, (c) and (d) dark and illuminated I-V curves respectively.

Electrical characteristics of the champion perovskite solar cell after good crystallization is displayed in Figure 5.4. We are able to obtain the diode J-V characteristics of the perovskite solar cell after the accurate implementations of hot N_2 blowing pipe and DMF DMSO ratios.

Table 5.1 summarizes the important parameters of our perovskite solar cell. Figure 5.5 shows the electrical power obtained with respect to applied voltage. P-V characteristic of the solar cell devices indicate the relationship of the maximum power delivered by the voltage of the solar cell. It is important to acknowledge that the calculation of the PCE of the solar cell can be derived from the P-V characteristic of the solar cell.

Table 5. 1 Parameters of champion solar cell

Efficiency (%)	0.63
FF (%)	37.7
V _{oc} (mV)	689.4
J _{sc} (mA/cm ²)	2.44
V _{max} (mV)	440.1
J _{max} (mA/cm ²)	1.44
I _{sc} (A)	0.000390
R _{sc} (Ω)	2815.9
R _{oc} (Ω)	676.78
Area (cm ²)	0.16
Incident Power (mW/cm ²)	100

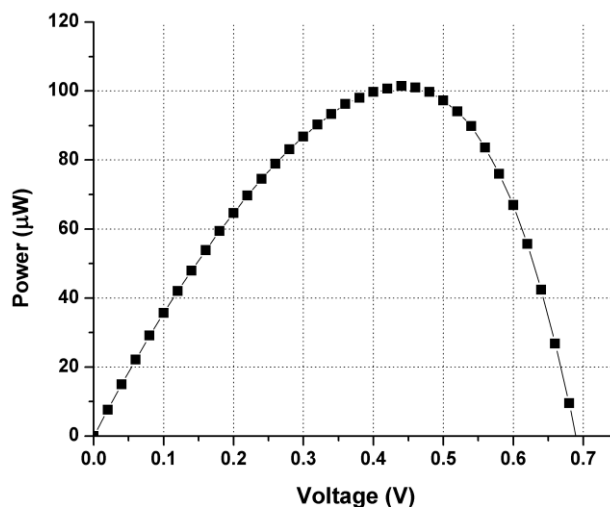


Figure 5.5. P-V characteristic of champion perovskite solar cell

5.4. Further Development of Spray Coating System

Since the system's initial day of operation, it has undergone significant development. In the past, the system required more human involvement; currently, it is

more automated. The system adjustments that can be done based on our observations will be detailed in this chapter's part in order to make the system better.

For a product to be commercially successful, reproducibility is essential. Spray deposition has some characteristics that make it difficult to reproduce, including ambient temperature and moisture. To increase repeatability, these elements should be kept in check by storing it in a glovebox.

In order for the system to be more automated and commercially viable, the hot nitrogen blowing gas, which we introduced as a novel system, can be changed from human control to computer control.

The single-step precursor solution deposited devices shows a characteristic of the inadequate surface coverage of the perovskite film resulting the undesired grain sizes, surface recombination, diffusion length, and carrier lifetime. All these parameters hinder the perovskite solar cell efficiency. As a result of this with the novel hot N₂ pipe and spraying system can be modified as a sequential deposition system as a route high-performance films⁹².

CHAPTER 6

CONCLUSION

Photovoltaic performances of spin-coated perovskite solar cell is potentially surpassed by those of scalable methods. As a result, much effort is being done to improve device efficiency by incorporating numerous novelties into scalable approaches.

In this thesis, hot N₂ gas blowing assisted spray deposition system is presented. Firstly, we examined the crystal and electronic structure, charge carrier dynamics, and mechanical properties of perovskites generally. Later we discussed hybrid halide perovskite solar cells. In order to do this we gave an introduction to the solid-state device theory, solar cells in general, and MAPb(I_{1-x})Br_x specifically.

In-depth explanations of the perovskite solar cell assembly process are provided, along with details on the characterization techniques employed. The experiments' power conversion rates, optical microscope, and SEM images were shared, and the outcomes were reviewed. The suggestions are discussed about how the system might be improved.

As a result of these studies, hot N₂ gas blowing assisted spray deposition was successfully employed as a scalable deposition method. We observed that the hot N₂ gas blowing can significantly advance the crystallization of the film. We also elucidated the effect of DMF : DMSO ratio on roughness of the film.

Finally, we discussed the possible approach how to enhance the photovoltaic parameters and feasibility of the perovskite solar cell by presenting two-step deposition system.

REFERENCES

- (1) Shafiee, S.; Topal, E. When Will Fossil Fuel Reserves Be Diminished? *Energy Policy* **2009**, 37 (1), 181–189. <https://doi.org/10.1016/j.enpol.2008.08.016>.
- (2) Hanjin, R. [Https://Upload.Wikimedia.Org/Wikipedia/Commons/](https://upload.wikimedia.org/wikipedia/commons/).
- (3) Geisthardt, R. M.; Topič, M.; Sites, J. R. Status and Potential of CdTe Solar-Cell Efficiency. *IEEE Journal of Photovoltaics* **2015**, 5 (4), 1217–1221. <https://doi.org/10.1109/JPHOTOV.2015.2434594>.
- (4) Metaferia, W.; Schulte, K. L.; Simon, J.; Johnston, S.; Ptak, A. J. Gallium Arsenide Solar Cells Grown at Rates Exceeding 300 Mm H–1 by Hydride Vapor Phase Epitaxy. *Nature Communications* **2019**, 10 (1). <https://doi.org/10.1038/s41467-019-11341-3>.
- (5) Scofield, J. H.; Duda, A.; Albin, D.; Ballardb, B. L.; Predeckib, P. K. Sputtered Molybdenum Bilayer Back Contact for Copper Indium Diselenide-Based Polycrystalline Thin-Film Solar Cells; 1995; Vol. 260.
- (6) Wenham, S. R.; Green, M. A.; Dericcs, P.; Sys, D.; On\,/. Invited Review Silicon Solar Cells; 1996; Vol. 4.
- (7) Andreani, L. C.; Bozzola, A.; Kowalczewski, P.; Liscidini, M.; Redorici, L. Silicon Solar Cells: Toward the Efficiency Limits. *Advances in Physics: X*. Taylor and Francis Ltd. January 1, 2019. <https://doi.org/10.1080/23746149.2018.1548305>.
- (8) Carey, G. H.; Abdelhady, A. L.; Ning, Z.; Thon, S. M.; Bakr, O. M.; Sargent, E. H. Colloidal Quantum Dot Solar Cells. *Chemical Reviews*. American Chemical Society December 9, 2015, pp 12732–12763. <https://doi.org/10.1021/acs.chemrev.5b00063>.
- (9) Nozik, A. J. *Quantum Dot Solar Cells*; 2002; Vol. 14.
- (10) Xue, R.; Zhang, J.; Li, Y.; Li, Y. Organic Solar Cell Materials toward Commercialization. *Small*. Wiley-VCH Verlag October 11, 2018. <https://doi.org/10.1002/smll.201801793>.
- (11) Board, E.; Abe, : A; Albertsson, A.-C.; Duncan, · R; Dušek, · K; de Jeu, · W H; Kausch, H.-H.; Kobayashi, · S; Lee, K.-S.; Leibler, · L; Long, T. E.; Manners, I.; Möller, · M; Nuyken, · O; Terentjev, · E M. 214 Advances in Polymer Science.
- (12) Bruner, C.; Dauskardt, R. Role of Molecular Weight on the Mechanical Device Properties of Organic Polymer Solar Cells. *Macromolecules* **2014**, 47 (3), 1117–1121. <https://doi.org/10.1021/ma402215j>.
- (13) Li, G.; Zhu, R.; Yang, Y. Polymer Solar Cells. *Nature Photonics*. March 2012, pp 153–161. <https://doi.org/10.1038/nphoton.2012.11>.

- (14) Özel, F.; Sarilmaz, A.; İstanbullu, B.; Aljabour, A.; Kuş, M.; Sönmezoğlu, S. Penternary Chalcogenides Nanocrystals as Catalytic Materials for Efficient Counter Electrodes in Dye-Synthesized Solar Cells. *Scientific Reports* **2016**, *6*. <https://doi.org/10.1038/srep29207>.
- (15) Shockley, W.; Queisser, H. J. Detailed Balance Limit of Efficiency of P-n Junction Solar Cells. *Journal of Applied Physics* **1961**, *32* (3), 510–519. <https://doi.org/10.1063/1.1736034>.
- (16) Park, B. wook; Seok, S. il. Intrinsic Instability of Inorganic–Organic Hybrid Halide Perovskite Materials. *Advanced Materials*. Wiley-VCH Verlag May 17, 2019. <https://doi.org/10.1002/adma.201805337>.
- (17) Cui, J.; Yuan, H.; Li, J.; Xu, X.; Shen, Y.; Lin, H.; Wang, M. Recent Progress in Efficient Hybrid Lead Halide Perovskite Solar Cells. *Science and Technology of Advanced Materials*. Institute of Physics Publishing June 1, 2015. <https://doi.org/10.1088/1468-6996/16/3/036004>.
- (18) Lu, H.; Krishna, A.; Zakeeruddin, S. M.; Grä, M.; Hagfeldt, A. IScience Compositional and Interface Engineering of Organic-Inorganic Lead Halide Perovskite Solar Cells. **2014**. <https://doi.org/10.1016/j.isci>.
- (19) Jeong, J.; Kim, M.; Seo, J.; Lu, H.; Ahlawat, P.; Mishra, A.; Yang, Y.; Hope, M. A.; Eickemeyer, F. T.; Kim, M.; Yoon, Y. J.; Choi, I. W.; Darwich, B. P.; Choi, S. J.; Jo, Y.; Lee, J. H.; Walker, B.; Zakeeruddin, S. M.; Emsley, L.; Rothlisberger, U.; Hagfeldt, A.; Kim, D. S.; Grätzel, M.; Kim, J. Y. Pseudo-Halide Anion Engineering for α -FAPbI₃ Perovskite Solar Cells. *Nature* **2021**, *592* (7854), 381–385. <https://doi.org/10.1038/s41586-021-03406-5>.
- (20) Thomson, S. Observing Phase Transitions in a Halide Perovskite Using Temperature Dependent Photoluminescence Spectroscopy Applications of Fluorescence Spectroscopy View Project APP LIC AT ION N O T E Observing Phase Transitions in a Halide Perovskite Using Temperature Dependent Photoluminescence Spectroscopy; 2018.
- (21) Kawamura, Y.; Mashiyama, H.; Hasebe, K. Structural Study on Cubic-Tetragonal Transition of CH₃NH₃PbI₃. *Journal of the Physical Society of Japan* **2002**, *71* (7), 1694–1697. <https://doi.org/10.1143/JPSJ.71.1694>.
- (22) Structure, C.; Caotnta, C.; Chothia, C.; Pauling, P. ; Pauling, P.; Coleman, L. W.; Little, O. E.; Bannard, R. A. I.; Cromer, D. T.; Mann, J. B.; Guttermson, R.; Robertson, B.; Stewart, R. F.; Davidson, E. R.; Simpson, W. T. The Classification of Tilted Octahedra in Perovskites; FORDAP, 1970; Vol. 225.
- (23) Kieslich, G.; Sun, S.; Cheetham, A. K. Solid-State Principles Applied to Organic–Inorganic Perovskites: New Tricks for an Old Dog. *Chemical Science* **2014**, *5* (12), 4712–4715. <https://doi.org/10.1039/c4sc02211d>.
- (24) Tan, W. L.; McNeill, C. R. X-Ray Diffraction of Photovoltaic Perovskites: Principles and Applications. *Applied Physics Reviews* **2022**, *9* (2), 021310. <https://doi.org/10.1063/5.0076665>.

- (25) Prasanna, R.; Gold-Parker, A.; Leijtens, T.; Conings, B.; Babayigit, A.; Boyen, H. G.; Toney, M. F.; McGehee, M. D. Band Gap Tuning via Lattice Contraction and Octahedral Tilting in Perovskite Materials for Photovoltaics. *J Am Chem Soc* **2017**, 139 (32), 11117–11124. <https://doi.org/10.1021/jacs.7b04981>.
- (26) Grote, C.; Berger, R. F. Strain Tuning of Tin-Halide and Lead-Halide Perovskites: A First-Principles Atomic and Electronic Structure Study. *Journal of Physical Chemistry C* **2015**, 119 (40), 22832–22837. <https://doi.org/10.1021/acs.jpcc.5b07446>.
- (27) Lee, J. H.; Bristowe, N. C.; Lee, J. H.; Lee, S. H.; Bristowe, P. D.; Cheetham, A. K.; Jang, H. M. Resolving the Physical Origin of Octahedral Tilting in Halide Perovskites. *Chemistry of Materials* **2016**, 28 (12), 4259–4266. <https://doi.org/10.1021/acs.chemmater.6b00968>.
- (28) Goesten, M. G.; Hoffmann, R. Mirrors of Bonding in Metal Halide Perovskites. *J Am Chem Soc* **2018**, 140 (40), 12996–13010. <https://doi.org/10.1021/jacs.8b08038>.
- (29) van Vechten, J. A.; Bergstresser\$\$, T. K. Electronic Structures of Semiconductor Alloys.
- (30) Hu, Z.; Lin, Z.; Su, J.; Zhang, J.; Chang, J.; Hao, Y. A Review on Energy Band-Gap Engineering for Perovskite Photovoltaics. *Solar RRL*. Wiley-VCH Verlag December 1, 2019. <https://doi.org/10.1002/solr.201900304>.
- (31) Connor, B. A.; Leppert, L.; Smith, M. D.; Neaton, J. B.; Karunadasa, H. I. Layered Halide Double Perovskites: Dimensional Reduction of Cs₂AgBiBr₆. *J Am Chem Soc* **2018**, 140 (15), 5235–5240. <https://doi.org/10.1021/jacs.8b01543>.
- (32) Herz, L. M. Charge-Carrier Dynamics in Organic-Inorganic Metal Halide Perovskites. *Annual Review of Physical Chemistry* **2016**, 67, 65–89. <https://doi.org/10.1146/annurev-physchem-040215-112222>.
- (33) Yang, Y.; Ostrowski, D. P.; France, R. M.; Zhu, K.; van de Lagemaat, J.; Luther, J. M.; Beard, M. C. Observation of a Hot-Phonon Bottleneck in Lead-Iodide Perovskites. *Nature Photonics* **2016**, 10 (1), 53–59. <https://doi.org/10.1038/nphoton.2015.213>.
- (34) Miyata, A.; Mitioglu, A.; Plochocka, P.; Portugall, O.; Wang, J. T. W.; Stranks, S. D.; Snaith, H. J.; Nicholas, R. J. Direct Measurement of the Exciton Binding Energy and Effective Masses for Charge Carriers in Organic-Inorganic Tri-Halide Perovskites. *Nature Physics* **2015**, 11 (7), 582–587. <https://doi.org/10.1038/nphys3357>.
- (35) Scholes, G. D.; Rumbles, G. WSPC-MATERIALS FOR SUSTAINABLE ENERGY-Reprint Volume Book-Trim Size:-11in x 8.5in; 2010.
- (36) Davies, C. L.; Filip, M. R.; Patel, J. B.; Crothers, T. W.; Verdi, C.; Wright, A. D.; Milot, R. L.; Giustino, F.; Johnston, M. B.; Herz, L. M. Bimolecular Recombination in Methylammonium Lead Triiodide Perovskite Is an Inverse

- Absorption Process. *Nature Communications* **2018**, 9 (1).
<https://doi.org/10.1038/s41467-017-02670-2>.
- (37) Elliott, R. J. Intensity of Optical Absorption by Excitons.
- (38) Stranks, S. D.; Burlakov, V. M.; Leijtens, T.; Ball, J. M.; Goriely, A.; Snaith, H. J. Recombination Kinetics in Organic-Inorganic Perovskites: Excitons, Free Charge, and Subgap States. *Physical Review Applied* **2014**, 2 (3).
<https://doi.org/10.1103/PhysRevApplied.2.034007>.
- (39) Richter, J. M.; Abdi-Jalebi, M.; Sadhanala, A.; Tabachnyk, M.; Rivett, J. P. H.; Pazos-Outón, L. M.; Gödel, K. C.; Price, M.; Deschler, F.; Friend, R. H. Enhancing Photoluminescence Yields in Lead Halide Perovskites by Photon Recycling and Light Out-Coupling. *Nature Communications* **2016**, 7.
<https://doi.org/10.1038/ncomms13941>.
- (40) Brenes, R.; Guo, D.; Osherov, A.; Noel, N. K.; Eames, C.; Hutter, E. M.; Pathak, S. K.; Niroui, F.; Friend, R. H.; Islam, M. S.; Snaith, H. J.; Bulović, V.; Savenije, T. J.; Stranks, S. D. Metal Halide Perovskite Polycrystalline Films Exhibiting Properties of Single Crystals. *Joule* **2017**, 1 (1), 155–167.
<https://doi.org/10.1016/j.joule.2017.08.006>.
- (41) Noel, N. K.; Abate, A.; Stranks, S. D.; Parrott, E. S.; Burlakov, V. M.; Goriely, A.; Snaith, H. J. Enhanced Photoluminescence and Solar Cell Performance via Lewis Base Passivation of Organic-Inorganic Lead Halide Perovskites. *ACS Nano* **2014**, 8 (10), 9815–9821. <https://doi.org/10.1021/nn5036476>.
- (42) DeQuilettes, D. W.; Jariwala, S.; Burke, S.; Ziffer, M. E.; Wang, J. T. W.; Snaith, H. J.; Ginger, D. S. Tracking Photoexcited Carriers in Hybrid Perovskite Semiconductors: Trap-Dominated Spatial Heterogeneity and Diffusion. *ACS Nano* **2017**, 11 (11), 11488–11496. <https://doi.org/10.1021/acsnano.7b06242>.
- (43) Braly, I. L.; Dequilettes, D. W.; Pazos-Outón, L. M.; Burke, S.; Ziffer, M. E.; Ginger, D. S.; Hillhouse, H. W. Hybrid Perovskite Films Approaching the Radiative Limit with over 90% Photoluminescence Quantum Efficiency. *Nature Photonics* **2018**, 12 (6), 355–361. <https://doi.org/10.1038/s41566-018-0154-z>.
- (44) Bella, F.; Griffini, G.; Correa-Baena, J. P.; Saracco, G.; Grätzel, M.; Hagfeldt, A.; Turri, S.; Gerbaldi, C. Improving Efficiency and Stability of Perovskite Solar Cells with Photocurable Fluoropolymers. *Science (1979)* **2016**, 354 (6309), 203–206. <https://doi.org/10.1126/science.aah4046>.
- (45) Ji, L. J.; Sun, S. J.; Qin, Y.; Li, K.; Li, W. Mechanical Properties of Hybrid Organic-Inorganic Perovskites. *Coordination Chemistry Reviews*. Elsevier B.V. July 15, 2019, pp 15–29. <https://doi.org/10.1016/j.ccr.2019.03.020>.
- (46) Ramirez, C.; Yadavalli, S. K.; Garces, H. F.; Zhou, Y.; Padture, N. P. Thermo-Mechanical Behavior of Organic-Inorganic Halide Perovskites for Solar Cells. *Scripta Materialia* **2018**, 150, 36–41.
<https://doi.org/10.1016/j.scriptamat.2018.02.022>.

- (47) Jacobsson, T. J.; Schwan, L. J.; Ottosson, M.; Hagfeldt, A.; Edvinsson, T. Determination of Thermal Expansion Coefficients and Locating the Temperature-Induced Phase Transition in Methylammonium Lead Perovskites Using X-Ray Diffraction. *Inorganic Chemistry* **2015**, 54 (22), 10678–10685. <https://doi.org/10.1021/acs.inorgchem.5b01481>.
- (48) Sun, S.; Fang, Y.; Kieslich, G.; White, T. J.; Cheetham, A. K. Mechanical Properties of Organic-Inorganic Halide Perovskites, $\text{CH}_3\text{NH}_3\text{PbX}_3$ ($\text{X} = \text{I}, \text{Br}$ and Cl), by Nanoindentation. *Journal of Materials Chemistry A* **2015**, 3 (36), 18450–18455. <https://doi.org/10.1039/c5ta03331d>.
- (49) Prasanna, R. PEROVSKITE TANDEM SOLAR CELLS A DISSERTATION SUBMITTED TO THE DEPARTMENT OF MATERIALS SCIENCE AND ENGINEERING AND THE COMMITTEE ON GRADUATE STUDIES OF STANFORD UNIVERSITY IN PARTIAL FULFILLMENT OF THE REQUIREMENTS FOR THE DEGREE OF DOCTOR OF PHILOSOPHY; 2019.
- (50) Rolston, N.; Bush, K. A.; Printz, A. D.; Gold-Parker, A.; Ding, Y.; Toney, M. F.; McGehee, M. D.; Dauskardt, R. H. Engineering Stress in Perovskite Solar Cells to Improve Stability. *Advanced Energy Materials* **2018**, 8 (29). <https://doi.org/10.1002/aenm.201802139>.
- (51) Jordan Hanania, K. S. J. D. https://energyeducation.ca/encyclopedia/Band_gap.
- (52) <https://www.allaboutcircuits.com/textbook/semiconductors/chpt-2/electrons-and-holes/>.
- (53) <https://byjus.com/physics/p-n-junction/>.
- (54) Husain, A. A. F.; Hasan, W. Z. W.; Shafie, S.; Hamidon, M. N.; Pandey, S. S. A Review of Transparent Solar Photovoltaic Technologies. *Renewable and Sustainable Energy Reviews*. Elsevier Ltd October 1, 2018, pp 779–791. <https://doi.org/10.1016/j.rser.2018.06.031>.
- (55) <https://pvpmc.sandia.gov/modeling-steps/2-dc-module-iv/diode-equivalent-circuit-models/>.
- (56) El-Ahmar, M. H.; El-Sayed, A. H. M.; Hemeida, A. M. Mathematical Modeling of Photovoltaic Module and Evaluate the Effect of Varoius Paramenters on Its Performance. In 2016 18th International Middle-East Power Systems Conference, MEPCON 2016 - Proceedings; Institute of Electrical and Electronics Engineers Inc., 2017; pp 741–746. <https://doi.org/10.1109/MEPCON.2016.7836976>.
- (57) Atiqur Rahman Mollick. <https://ecowowlife.com/fill-factor-of-solar-cell/>.
- (58) <https://www.universitywafer.com/what-is-the-shockley-queisser-limit.html>.
- (59) Ghosh, B. K.; Weoi, C. N. J.; Islam, A.; Ghosh, S. K. Recent Progress in Si Hetero-Junction Solar Cell: A Comprehensive Review. *Renewable and Sustainable Energy Reviews*. Elsevier Ltd February 1, 2018, pp 1990–2004. <https://doi.org/10.1016/j.rser.2017.07.022>.

- (60) Kojima, A.; Teshima, K.; Shirai, Y.; Miyasaka, T. Organometal Halide Perovskites as Visible-Light Sensitizers for Photovoltaic Cells. *J Am Chem Soc* **2009**, 131 (17), 6050–6051. <https://doi.org/10.1021/ja809598r>.
- (61) Zhao, Y.; Zhu, K. Organic-Inorganic Hybrid Lead Halide Perovskites for Optoelectronic and Electronic Applications. *Chemical Society Reviews*. Royal Society of Chemistry February 7, 2016, pp 655–689. <https://doi.org/10.1039/c4cs00458b>.
- (62) Suarez, B.; Gonzalez-Pedro, V.; Ripolles, T. S.; Sanchez, R. S.; Otero, L.; Mora-Sero, I. Recombination Study of Combined Halides (Cl, Br, I) Perovskite Solar Cells. *Journal of Physical Chemistry Letters* **2014**, 5 (10), 1628–1635. <https://doi.org/10.1021/jz5006797>.
- (63) Miyano, K.; Tripathi, N.; Yanagida, M.; Shirai, Y. Lead Halide Perovskite Photovoltaic as a Model P-i-n Diode. *Accounts of Chemical Research* **2016**, 49 (2), 303–310. <https://doi.org/10.1021/acs.accounts.5b00436>.
- (64) Stranks, S. D.; Eperon, G. E.; Grancini, G.; Menelaou, C.; Alcocer, M. J. P.; Leijtens, T.; Herz, L. M.; Petrozza, A.; Snaith, H. J. Electron-Hole Diffusion Lengths Exceeding 1 Micrometer in an Organometal Trihalide Perovskite Absorber. *Science* (1979) **2013**, 342 (6156), 341–344. <https://doi.org/10.1126/science.1243982>.
- (65) Dong, Q.; Fang, Y.; Shao, Y.; Mulligan, P.; Qiu, J.; Cao, L.; Huang, J. Electron-Hole Diffusion Lengths > 175 Mm in Solution-Grown CH₃NH₃PbI₃ Single Crystals. *Science* (1979) **2015**, 347 (6225), 967–970. <https://doi.org/10.1126/science.aaa5760>.
- (66) Giorgi, G.; Fujisawa, J. I.; Segawa, H.; Yamashita, K. Small Photocarrier Effective Masses Featuring Ambipolar Transport in Methylammonium Lead Iodide Perovskite: A Density Functional Analysis. *Journal of Physical Chemistry Letters* **2013**, 4 (24), 4213–4216. <https://doi.org/10.1021/jz4023865>.
- (67) Stranks, S. D.; Snaith, H. J. Metal-Halide Perovskites for Photovoltaic and Light-Emitting Devices. *Nature Nanotechnology*. Nature Publishing Group May 7, 2015, pp 391–402. <https://doi.org/10.1038/nnano.2015.90>.
- (68) DeQuilettes, D. W.; Vorpahl, S. M.; Stranks, S. D.; Nagaoka, H.; Eperon, G. E.; Ziffer, M. E.; Snaith, H. J.; Ginger, D. S. Impact of Microstructure on Local Carrier Lifetime in Perovskite Solar Cells. *Science* (1979) **2015**, 348 (6235), 683–686. <https://doi.org/10.1126/science.aaa5333>.
- (69) Jena, A. K.; Kulkarni, A.; Miyasaka, T. Halide Perovskite Photovoltaics: Background, Status, and Future Prospects. *Chemical Reviews* **2019**, 119 (5), 3036–3103. <https://doi.org/10.1021/acs.chemrev.8b00539>.
- (70) Zhang, C.; Luan, W.; Yin, Y. High Efficient Planar-Heterojunction Perovskite Solar Cell Based on Two-Step Deposition Process. In *Energy Procedia*; Elsevier Ltd, 2017; Vol. 105, pp 793–798. <https://doi.org/10.1016/j.egypro.2017.03.391>.

- (71) Chouhan, A. S.; Jasti, N. P.; Hadke, S.; Raghavan, S.; Avasthi, S. Large Grained and High Charge Carrier Lifetime CH₃NH₃PbI₃ Thin-Films: Implications for Perovskite Solar Cells. *Current Applied Physics* **2017**, 17 (10), 1335–1340. <https://doi.org/10.1016/j.cap.2017.07.005>.
- (72) Bi, Y.; Hutter, E. M.; Fang, Y.; Dong, Q.; Huang, J.; Savenije, T. J. Charge Carrier Lifetimes Exceeding 15 Ms in Methylammonium Lead Iodide Single Crystals. *Journal of Physical Chemistry Letters* **2016**, 7 (5), 923–928. <https://doi.org/10.1021/acs.jpclett.6b00269>.
- (73) Pонсеа, С. С.; Савениже, Т. І.; Абделлах, М.; Ченг, К.; Ярцев, А.; Пашер, Т.; Харлан, Т.; Чабера, П.; Пуллерітс, Т.; Степанов, А.; Вольф, І. Р.; Сундстром, В. Органометалічні хлориди перовські сонячні матеріали обґрунтовано: Ультрафаста генерація заряду, високі та мікростайд-довгі балансовані мобільності, та повільна рекомбінація. *J Am Chem Soc* **2014**, 136 (14), 5189–5192. <https://doi.org/10.1021/ja412583t>.
- (74) Johnston, M. B.; Herz, L. M. Hybrid Perovskites for Photovoltaics: Charge-Carrier Recombination, Diffusion, and Radiative Efficiencies. *Accounts of Chemical Research* **2016**, 49 (1), 146–154. <https://doi.org/10.1021/acs.accounts.5b00411>.
- (75) Xing, G.; Mathews, N.; Sun, S.; Lim, S. S.; Lam, Y. M.; Grätzel, M.; Mhaisalkar, S.; Sum, T. C. Long-Range Balanced Electron-and Hole-Transport Lengths in Organic-Inorganic CH₃NH₃PbI₃. *Science (1979)* **2013**, 342 (6156), 344–347. <https://doi.org/10.1126/science.1243167>.
- (76) Green, M. A.; Ho-Baillie, A.; Snaith, H. J. The Emergence of Perovskite Solar Cells. *Nature Photonics*. Nature Publishing Group 2014, pp 506–514. <https://doi.org/10.1038/nphoton.2014.134>.
- (77) Zhou, Y.; Game, O. S.; Pang, S.; Padture, N. P. Microstructures of Organometal Trihalide Perovskites for Solar Cells: Their Evolution from Solutions and Characterization. *Journal of Physical Chemistry Letters* **2015**, 6 (23), 4827–4839. <https://doi.org/10.1021/acs.jpclett.5b01843>.
- (78) Liu, B.; Wang, S.; Ma, Z.; Ma, J.; Ma, R.; Wang, C. High-Performance Perovskite Solar Cells with Large Grain-Size Obtained by the Synergy of Urea and Dimethyl Sulfoxide. *Applied Surface Science* **2019**, 467–468, 708–714. <https://doi.org/10.1016/j.apsusc.2018.10.141>.
- (79) Zhou, Y.; Yang, M.; Game, O. S.; Wu, W.; Kwun, J.; Strauss, M. A.; Yan, Y.; Huang, J.; Zhu, K.; Padture, N. P. Manipulating Crystallization of Organolead Mixed-Halide Thin Films in Antisolvent Baths for Wide-Bandgap Perovskite Solar Cells. *ACS Applied Materials and Interfaces* **2016**, 8 (3), 2232–2237. <https://doi.org/10.1021/acsami.5b10987>.
- (80) Zhou, X.; Zhang, Y.; Kong, W.; Hu, M.; Zhang, L.; Liu, C.; Li, X.; Pan, C.; Yu, G.; Cheng, C.; Xu, B. Crystallization Manipulation and Morphology Evolution for Highly Efficient Perovskite Solar Cell Fabrication: Via Hydration Water

- Induced Intermediate Phase Formation under Heat Assisted Spin-Coating. *Journal of Materials Chemistry A* **2018**, 6 (7), 3012–3021. <https://doi.org/10.1039/c7ta08947c>.
- (81) <https://www.findlight.net/blog/2017/12/15/ar-coating-techniques/>.
- (82) Yang, M.; Li, Z.; Reese, M. O.; Reid, O. G.; Kim, D. H.; Siol, S.; Klein, T. R.; Yan, Y.; Berry, J. J.; van Hest, M. F. A. M.; Zhu, K. Perovskite Ink with Wide Processing Window for Scalable High-Efficiency Solar Cells. *Nature Energy* **2017**, 2 (5). <https://doi.org/10.1038/nenergy.2017.38>.
- (83) Tang, S.; Deng, Y.; Zheng, X.; Bai, Y.; Fang, Y.; Dong, Q.; Wei, H.; Huang, J. Composition Engineering in Doctor-Blading of Perovskite Solar Cells. *Advanced Energy Materials* **2017**, 7 (18). <https://doi.org/10.1002/aenm.201700302>.
- (84) Li, Z.; Klein, T. R.; Kim, D. H.; Yang, M.; Berry, J. J.; van Hest, M. F. A. M.; Zhu, K. Scalable Fabrication of Perovskite Solar Cells. *Nature Reviews Materials*. Nature Publishing Group March 27, 2018. <https://doi.org/10.1038/natrevmats.2018.17>.
- (85) Jabari, E.; Liravi, F.; Toyserkani, E. Additive Manufacturing of Silicone Structures View Project Material Jetting of Carbon-Based Functional Inks View Project. **2019**. <https://doi.org/10.1088/2053-1583/ab29b2/meta>.
- (86) Howard, I. A.; Abzieher, T.; Hossain, I. M.; Eggers, H.; Schackmar, F.; Ternes, S.; Richards, B. S.; Lemmer, U.; Paetzold, U. W. Coated and Printed Perovskites for Photovoltaic Applications. *Advanced Materials* **2019**, 31 (26). <https://doi.org/10.1002/adma.201806702>.
- (87) Barrows, A. T.; Pearson, A. J.; Kwak, C. K.; Dunbar, A. D. F.; Buckley, A. R.; Lidzey, D. G. Efficient Planar Heterojunction Mixed-Halide Perovskite Solar Cells Deposited via Spray-Deposition. *Energy and Environmental Science* **2014**, 7 (9), 2944–2950. <https://doi.org/10.1039/c4ee01546k>.
- (88) Huang, H.; Shi, J.; Zhu, L.; Li, D.; Luo, Y.; Meng, Q. Two-Step Ultrasonic Spray Deposition of CH₃NH₃PbI₃ for Efficient and Large-Area Perovskite Solar Cell. *Nano Energy* **2016**, 27, 352–358. <https://doi.org/10.1016/j.nanoen.2016.07.026>.
- (89) Cai, H.; Liang, X.; Ye, X.; Su, J.; Guan, J.; Yang, J.; Liu, Y.; Zhou, X.; Han, R.; Ni, J.; Li, J.; Zhang, J. High Efficiency over 20% of Perovskite Solar Cells by Spray Coating via a Simple Process. *ACS Applied Energy Materials* **2020**, 3 (10), 9696–9702. <https://doi.org/10.1021/acsaem.0c01129>.
- (90) Heo, J. H.; Lee, M. H.; Jang, M. H.; Im, S. H. Highly Efficient CH₃NH₃PbI₃-xCl_x Mixed Halide Perovskite Solar Cells Prepared by Re-Dissolution and Crystal Grain Growth via Spray Coating. *Journal of Materials Chemistry A* **2016**, 4 (45), 17636–17642. <https://doi.org/10.1039/c6ta06718b>.
- (91) Watthage, S. C.; Song, Z.; Phillips, A. B.; Heben, M. J. Evolution of Perovskite Solar Cells. In *Perovskite Photovoltaics: Basic to Advanced Concepts and*

Implementation; Elsevier, 2018; pp 43–88. <https://doi.org/10.1016/B978-0-12-812915-9.00003-4>.

- (92) Burschka, J.; Pellet, N.; Moon, S. J.; Humphry-Baker, R.; Gao, P.; Nazeeruddin, M. K.; Grätzel, M. Sequential Deposition as a Route to High-Performance Perovskite-Sensitized Solar Cells. *Nature* **2013**, 499 (7458), 316–319. <https://doi.org/10.1038/nature12340>.